PHYSICAL REVIEW B **94**, 174514 (2016)

Roadmap to Majorana surface codes

S. Plugge,[1,2] L. A. Landau,[3] E. Sela,[3] A. Altland,[4] K. Flensberg,[2] and R. Egger[1]

[1]*Institut für Theoretische Physik, Heinrich-Heine-Universität, D-40225 Düsseldorf, Germany*

[2]*Center for Quantum Devices and Station Q Copenhagen, Niels Bohr Institute, University of Copenhagen, Universitetsparken 5, DK-2100 Copenhagen, Denmark*

[3]*Raymond and Beverly Sackler School of Physics and Astronomy, Tel-Aviv University, Tel Aviv 69978, Israel*

[4]*Institut für Theoretische Physik, Universität zu Köln, Zülpicher Str. 77, D-50937 Köln, Germany*

(Received 27 June 2016; published 23 November 2016)

Surface codes offer a very promising avenue towards fault-tolerant quantum computation. We argue that two-dimensional interacting networks of Majorana bound states in topological superconductor/semiconductor heterostructures hold several key advantages in that direction, concerning both the hardware realization and the actual operation of the code. We here discuss how topologically protected logical qubits in this Majorana surface code architecture can be defined, initialized, manipulated, and read out. All physical ingredients needed to implement these operations are routinely used in topologically trivial quantum devices. By means of quantum interference terms in linear conductance measurements, single-electron pumping protocols, and gate-tunable tunnel barriers, the full set of quantum gates required for universal quantum computation can be achieved. In particular, we show that designated multistep pumping sequences via tunnel-coupled quantum dots realize high-fidelity ancilla states for phase gates.

DOI: 10.1103/PhysRevB.94.174514

I. INTRODUCTION

Surface code architectures are currently being recognized as potentially very powerful platforms for quantum information processing (QIP) and universal quantum computation [1–11]. Based on relatively simple two-dimensional (2D) array structures, the distinguishing hallmark of code-based QIP is redundancy: A rather small number of logical (or information) qubits is integrated into the background of a much larger number of physical qubits. The latter are built from local combinations of elementary hardware qubits and act as so-called stabilizers of the code, i.e., they are subject to readout operations projecting the system to a well-defined code state. The encoding of relatively few logical qubits into a large entangled code space provides a highly potent resource for error detection/correction and fault tolerance in quantum operations. In fact, as long as the microscopic error probability for physical qubit manipulations stays below a rather benign threshold of order $\approx 1\%$ [8–11], logical qubits enjoy a topological protection with exponentially small error rates for increasing ratio of physical to logical qubits [4]. Somewhat less obviously, this encoding strategy also makes the boundaries between hard- and software less rigid than in other QIP approaches. For example, whether a given physical qubit acts as stabilizer or as storage space for logical information in each computation cycle will be decided by the code protocols and the applied measurement pattern. To a certain degree, error handling can then be reduced to simply tracking errors by classical software. An excellent and detailed review of the surface code approach to quantum computing has been given by Fowler *et al.* [10].

However, there is a price to be paid for the high levels of flexibility and fault tolerance in QIP based on surface codes, namely the tremendous hardware overhead introduced by the code space. Referring to Refs. [8–10] for detailed estimates, the realization of a useful system (allowing for well-protected QIP) of just a few dozen logical qubits might require to assemble thousands of physical qubits. This means that maximal efficiency will be critically important to the design of scalable surface code platforms, raising questions both concerning the physical realization of the code and, equally important, its operation.

Realization. What levels of physical qubit integration can be reached at nanoscopic or mesoscopic length scales? How much hardware overhead is required to define, manipulate, and read out logical qubit states? To what extent is the manipulation of individual qubits detrimental to the operation of the code, say, with regard to generated heat or radiation levels? If external electromagnetic fields are necessary, can their cumulative effects be kept at bay when large numbers of qubits are integrated?

Operation. Can one address qubits with logarithmic efficiency [11], e.g., via noninvasive multiplexer schemes? Recalling that code-based QIP relies on the repeated readout of many stabilizers, can measurements be performed at sufficient speed, say, with a cycle time of a few microseconds? Can the full set of logical gates required for universal quantum computation be realized at tolerable efforts? How can one avoid decay and dephasing of qubits due to residual interactions, e.g., with readout or manipulation devices, or between qubits themselves?

In Ref. [12], we have argued that topological hybrid superconductor/semiconductor architectures featuring Majorana bound states might evolve into a platform performing favorably with regard to many of the above criteria. (For reviews on Majorana states in such devices, see Refs. [13–16]. Majorana surface codes are also discussed in Refs. [17–21].) Given that not even a single topological semiconductor qubit has been realized so far, this assertion may seem presumptuous. However, current striking developments in the materials foundations of topological semiconductor devices, including experimentally observed signatures of Majorana states, see Refs. [22–28], give rise to cautious optimism that the realization of functioning device architectures is but a matter of time. Two developments in

particular seem of key importance. First, progress in the growth of high-quality superconductor/semiconductor interfaces has been instrumental to the formation of hard excitation gaps and to the protection of Majorana states [23–27]. Second, the successful realization of 2D superconductor/semiconductor heterostructures [28,29] suggests that it may be advantageous to switch from nanowire architectures to genuine 2D layouts. For concreteness, we describe the wire construction below. However, we do not expect that the analogous formulation of a 2D architecture will differ on a conceptual level. Once realized, either structure will be accessible in terms of the full spectrum of device manipulations and measurement protocols of mesoscopic quantum electronics, including (i) quantum interferometry by point contact measurements of the linear conductance, (ii) access by quantum dots that allow one to pump single electrons on and off the code, and (iii) the option to connect and disconnect qubits from the code by tuning selected voltages.

We have sketched basic aspects of the access hardware and some elementary code operations in Ref. [12], including stabilizer readout and the controlled creation of anyonic excitations. The present paper paves the way along a different direction, namely how to operate an experimentally feasible Majorana-based surface code platform in terms of a few highly efficient basal quantum operations. Elemental gates for Majorana surface codes and their gate-circuit implementations have been described before in Refs. [11,17–19]. Below we address the initialization, manipulation, protection, and readout of logical qubits in our device architecture, up to and including a set of universal gates for fault-tolerant quantum computation. Some of our gate constructions are inspired by earlier ideas (e.g., for the controlled-NOT and Hadamard gates), but others are altogether new, in particular, for the $\hat{S}$- and $\hat{T}$-phase gates. Our $\hat{S}$-gate implementation employs only simple measurement-induced qubit manipulations, while for the $\hat{T}$ gate, we devise multistep single-electron pumping protocols. The latter are guaranteed to yield a phase gate and can be used to directly generate high-fidelity ancilla states. We expect this feature to be especially useful in practice since one can thereby reduce, or even completely avoid, the large overhead introduced by magic state distillation [5].

All QIP protocols presented in what follows rely on the unique measurement-based manipulation and quantum interference capabilities offered by our code architecture. Their high efficiency can be traced back to the underlying topological nature of the elementary qubits together with the fact that the non-Abelian braiding of Majorana fermions is not needed to operate a Majorana surface code [11,17–19], in contrast to most alternative approaches to Majorana-based quantum computing [30–40]. The latter point also implies that the experimentally challenging topological T junctions are not needed in our approach. We stress that none of our basal operations requires significant overhead compared to the hardware and manipulations already needed for the basic code structures. All its operations are performed through conductance measurements, pumping protocols, and/or gate voltage changes. Our logical gate implementations differ, and sometimes simpler, than those suggested for bosonic codes [10,41–45] or other Majorana code realizations [18–20]. In view of the challenging demands on the efficiency of elementary quantum operations, we believe that the above signatures will be of critical importance for the successful realization of large-scale Majorana-based quantum computation platforms.

Before entering a detailed discussion in Sec. II, we give a brief synopsis of our architecture. Its skeleton structure is defined by a regular square lattice of so-called Majorana-Cooper boxes (MCBs) linked by tunnel bridges, see Fig. 1. Each MCB corresponds to two topological semiconductor nanowires proximitized by a common, floating superconducting island. The nanowires in the setup of Fig. 1 are parallel, which means that a homogeneous parallel magnetic Zeeman field can synchronously drive them into a topological phase [13–15]. Within the topological phase, each wire supports Majorana zero-energy end states, giving rise to a total of four states per MCB. Each Majorana state is assumed to be individually tunnel coupled to an external lead electrode and to a quantum dot (or single-electron transistor). We augment the hardware described in Ref. [12] by local interference links between nearby pairs of external leads. Such links can be realized as gate-tunable tunnel bridges that may be switched on and off as needed. Once in place, they will allow for interferometric transport measurements of Majorana strings (e.g., bilinears), which will in turn be instrumental to the manipulation of logical operators. Assuming a large capacitive charging energy, backgate voltages may now be tuned to effect charge quantization on each MCB [46–48]. The low-energy state of a given MCB is then equivalently described by an effective spin-1/2 degree of freedom [49–54]. These spins are the elementary hardware qubits of our system and can be described by Pauli matrices $(\hat{x},\hat{y},\hat{z})_l$ for MCB no. l. The fractionalization of spins into Majorana components, see Eq. (2), in turn allows for the unique spatially nonlocal addressing and readout capabilities exploited in our QIP protocols.

Including tunnel bridges linking neighboring MCBs into the checkerboard pattern of Fig. 1, spin-1/2 ring-exchange processes around the elementary plaquettes (loops) of the 2D lattice are generated. These may be described as products of MCB Pauli operators, either of four $\hat{z}_l$ or of four $\hat{x}_l$. The emerging two types of composite physical qubits, denoted by $\hat{Z}$ and $\hat{X}$ in Fig. 1, are the stabilizers of the surface code. Physically, one may think of the stabilizer qubit as the $\mathbb{Z}_2$-valued flux captured by the lattice ring-exchange processes.

Our basic approach to the repeated stabilizer measurement is quantum interferometry (cf. Refs. [55,56]): Current passing through two terminals adjacent to a plaquette can pass around this loop in clockwise or anticlockwise direction, and the interference between these paths identifies qubit states through conductance measurements. This single-step measurement protocol neither requires ancilla qubits, cf. also Refs. [19,20], nor hardware beyond that already present in the system. For nontopological device architectures, such point-contact conductance interferometry techniques are routinely used and their extension to Majorana islands [26] are not expected to create huge difficulties. Via the above-mentioned interference links, similar interferometric transport measurements can determine the eigenvalues of arbitrary Majorana bilinears and strings, including those of the qubit operators $(\hat{x},\hat{y},\hat{z})_l$.

It is obvious that experimental efforts will first focus on structures simpler than that of a large 2D code. This includes

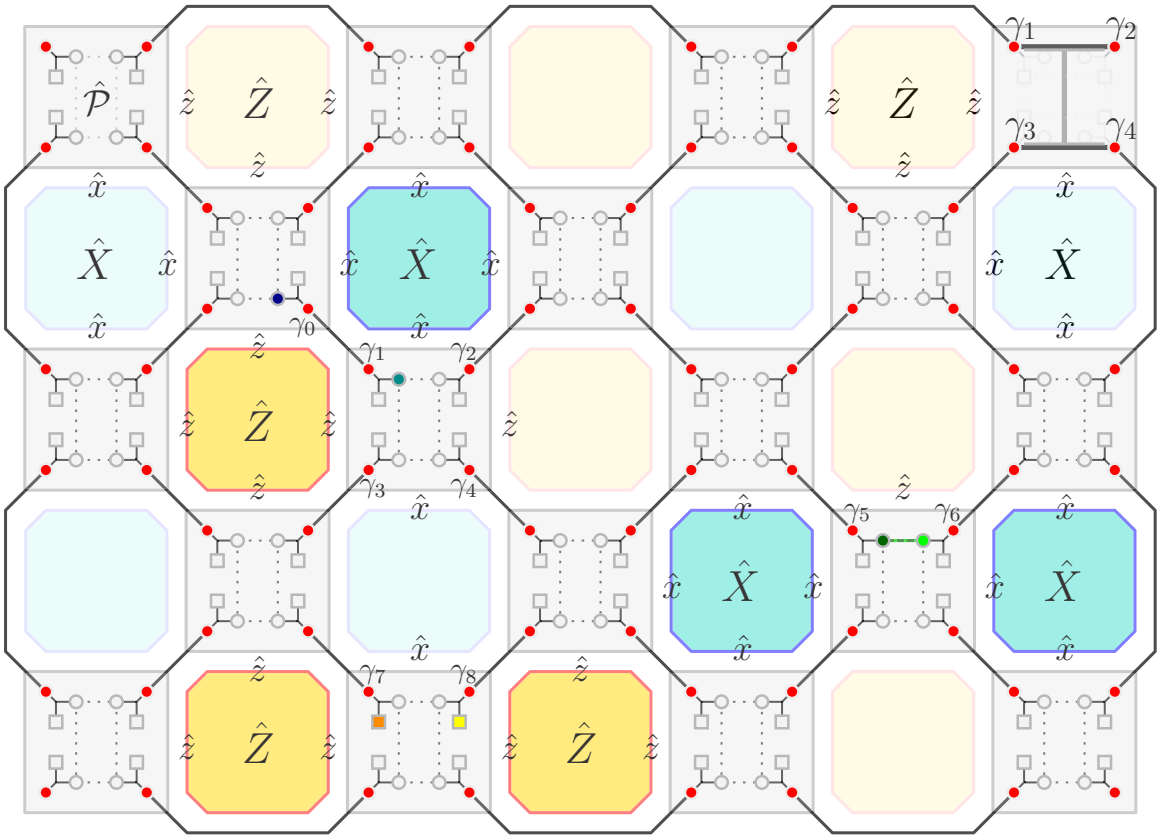

FIG. 1. Schematic Majorana code architecture with 18 MCBs (light gray). The MCB is a floating superconducting island with four Majorana end states $\gamma_{j=1,\ldots,4}$ (red dots) of topological semiconductor wires, which can be implemented, e.g., as 90° rotated H-shaped device [12] (for an illustration, see top right corner). The fermion parity on a given MCB, $\hat{\mathcal{P}} = \gamma_1\gamma_2\gamma_3\gamma_4$, is constrained by Coulomb blockade, see Eq. (1), and Majorana bilinears define Pauli operators $(\hat{x},\hat{z})$, see Eq. (2). Majorana states on neighboring MCBs are linked by tunnel bridges (solid black lines). Away from (near) boundaries, minimal plaquettes involve products of eight (six) Majoranas. These stabilizers are either of type $\hat{X}$ (blue) or $\hat{Z}$ (yellow), corresponding to products of four (three) $\hat{x}$ or $\hat{z}$ operators, respetively, see Eq. (6). Note that near the top/bottom Z-type (left/right X-type) code boundaries, only $\hat{Z}$ ($\hat{X}$) stabilizers appear. Stabilizer eigenvalues are read out by conductance measurements, see Eq. (8). By using leads (small circles) tunnel coupled to γ_0 and γ_1, respectively, one measures the two adjacent (colored) stabilizers. Majorana bilinears can be read out by adding interference links between leads (dotted lines). By using leads attached to γ_5 and γ_6, we can measure $\hat{z} = i\gamma_5\gamma_6$, cf. Eq. (10). This Pauli operator readout affects the neigboring (blue) $\hat{X}$ stabilizers, which anticommute with $\hat{z}$. By pumping a single electron between two quantum dots (indicated by squares), one generates a string operator. With dots attached to γ_7 and γ_8, the latter is $\hat{x} = i\gamma_7\gamma_8$ and flips the two adjacent (yellow) $\hat{Z}$ stabilizers.

1D chains that may implement so-called repetition codes [45] which do not achieve the full computational power of a 2D surface code. Nonetheless, many of the manipulation and readout tools needed for QIP in the 2D code can already be implemented and tested using small MCB chains or arrays. We note that recent theoretical work [57] has examined related models.

The remainder of this paper is structured as follows. We start out in Sec. II with a discussion of the different hardware hierarchies defining our code architecture. In order to keep the paper self-contained, Sec. II also summarizes the key results of Ref. [12]. In Sec. III, we show how logical qubits are defined. Basal quantum operations are discussed in the central Sec. IV, where we demonstrate how logical qubits can be initialized, moved, braided, manipulated, and read out in this architecture. To that end, we will also introduce a powerful class of generalized pumping protocols. In Sec. IV F, we offer an analysis of potential challenges and/or error sources. With those basal operations at hand, the implementation of a full set of quantum gates for universal quantum computation is possible using established quantum circuits [10,19,58], see Sec. V. The paper ends with concluding remarks in Sec. VI. Finally, we note that we often use units with $\hbar = 1$ below.

II. MAJORANA SURFACE CODE HARDWARE

A. Majorana-Cooper box

The elementary unit of our architecture is the MCB, described in detail in Refs. [49–54] and schematically illustrated in Fig. 1. In the following we briefly introduce the MCB, where the emphasis will be on its subsequent integration into a surface code structure. Interested readers may find a concrete proposal for the hardware layout of an MCB in Ref. [12]. An isolated MCB consists of a mesoscopic s-wave superconducting island in contact to two semiconductor nanowires with strong spin-orbit interaction (e.g., InAs or InSb). On each wire a pairing gap is induced by the proximity effect, which we assume to be so large that continuum quasiparticles can be ignored. Residual

quasiparticle poisoning effects are discussed in Sec. IV F. When subjected to a sufficiently strong Zeeman field, the wires enter a topological regime with Majorana bound states near their ends [13–15]. We here consider wires long enough that direct tunnel couplings between different end states are negligible, but finite-coupling effects are briefly addressed in Sec. IV F.

In effect, as illustrated in Fig. 1, we then have four zero-energy Majorana states described by Hermitian operators, $\gamma_j = \gamma_j^\dagger$, which satisfy a Clifford anticommutator algebra, $\{\gamma_j,\gamma_{j'}\} = 2\delta_{jj'}$ [13–15]. Recalling that a conventional fermion can be built from two Majorana fermions, the presence of four zero-energy Majorana states implies a fourfold degeneracy. This degeneracy gets lifted by the Coulomb blockade, which has to be taken into account because we consider a floating (not grounded) island with a large single-electron charging energy $E_C \approx 1$ meV [26]. For notational simplicity, we shall consider the same E_C for all MCBs below. In what follows, the effective energy scales of the problem are assumed to be below both the proximity-induced pairing gap and the charging energy.

Since Cooper pairs and Majorana fermions both represent zero-energy states, the Hamiltonian of a single MCB contains only the capacitive charging energy contribution, $H_{\rm MCB} = E_C(\hat{N} - n_g)^2$, where the parameter n_g can be tuned by a backgate voltage. The operator $\hat{N}$ has integer eigenvalues (N) and counts the fermion number on the MCB. Within our low-energy framework, these fermions are either bound in Cooper pairs or belong to the Majorana sector. Under Coulomb valley conditions, i.e., for n_g close to integer values, the charging energy then enforces a well-defined ground-state value for N, even if weak tunnel couplings to other code parts are present. Depending on our choice for n_g, this value is either even or odd. Since the number of electrons bound in Cooper pairs is always even, a parity constraint emerges in the Majorana sector [49],

$$\hat{\mathcal{P}} = \gamma_1\gamma_2\gamma_3\gamma_4 = (-1)^N = \pm 1, \tag{1}$$

reducing the fourfold degeneracy to a twofold degeneracy. With charge fluctuations being frozen out by Coulomb blockade, the low-energy dynamics of the MCB is then described by an effective spin-1/2 variable. The associated Pauli operators $(\hat{x},\hat{y},\hat{z})$ correspond to bilinear combinations of Majorana operators and afford the representation [49,53,54]

$$\hat{x} = i\gamma_1\gamma_2, \quad \hat{y} = i\gamma_2\gamma_3, \quad \hat{z} = i\gamma_1\gamma_3. \tag{2}$$

Note that this representation is consistent with standard Pauli matrix relations, $\hat{x}\hat{y} = i\hat{z}$ and so on. Using the parity constraint (1), each Pauli operator can equivalently be expressed by the complementary pair of Majorana operators, e.g., $\hat{x} = \mp i\gamma_3\gamma_4$. For 2D arrays of MCBs, it is convenient to choose an alternating representation as illustrated in Fig. 1. For MCB l, Pauli operators $(\hat{x}_l,\hat{y}_l,\hat{z}_l)$ are assigned for l in an odd column (containing three MCBs in Fig. 1), but the unitarily transformed representation $(\hat{z}_l,-\hat{y}_l,\hat{x}_l)$ will be used for even columns (with two MCBs in Fig. 1). This convention leads to a maximally transparent representation of stabilizer operators in terms of MCB Pauli operators, see Eq. (6) below.

The tunnel coupling between Majorana state j of an MCB and an attached lead or quantum dot with fermion operator Ψ is described by the tunneling Hamiltonian [46,47,54]

$$H_{\rm t} = t_j\Psi^\dagger e^{-i\hat{\varphi}/2}\gamma_j + \text{H.c.}, \tag{3}$$

where t_j is a complex tunneling amplitude and the phase operator $\hat{\varphi}$ is conjugate to the number operator, $[\hat{\varphi},\hat{N}] = 2i$. The factor of two means that $e^{i\hat{\varphi}}$ creates a Cooper pair, $N \to N+2$, and hence the out-tunneling process contained in Eq. (3) annihilates a single electron charge on the island. The representation (3) manifestly splits the tunneling process into a transfer of charge and the charge-neutral Majorana dynamics.

B. MCB network

We next consider a network of MCBs as shown in Fig. 1, where MCB l has the fluctuating superconducting phase φ_l. Neighboring MCBs are coupled through short tunnel bridges connecting specific pairs of Majorana states $(\gamma_l,\gamma_{l'})$. Describing each contact in terms of the tunneling Hamiltonian (3) with tunnel amplitude t_l between γ_l and the respective bridge fermion Ψ_l, the effective MCB-MCB tunneling Hamiltonian follows by second-order perturbation theory,

$$H_{\rm tun} = -\frac{t_{ll'}}{2}e^{i(\hat{\varphi}_l-\hat{\varphi}_{l'})/2}\gamma_l\gamma_{l'} + \text{H.c.}, \tag{4}$$

where $t_{ll'} \simeq t_l^* t_{l'} G(l,l')$ contains the low-energy fermion propagator of the bridge. For a sufficiently short bridge, retardation effects in this propagator are negligible and the coupling constants $t_{ll'}$ are effectively time- and/or energy-independent. As an example with the above properties, one may think of tunnel bridges that include short nonproximitized nanowire segments connecting adjacent MCBs. Such small-sized connectors typically form junction dots, i.e., few-level systems where electrostatic gating makes the $t_{ll'}$ couplings tunable. For $|t_{ll'}| \gtrsim 0.33E_C$, the ground state of the system enters a frustrated 2D Ising phase which is not useful for QIP purposes [18]. We therefore focus on the regime $|t_{ll'}| \ll E_C$ throughout.

The presence of the exponentiated phase operators in Eq. (4) indicates that a single tunneling process kicks both participating MCBs out of their respective charge ground states, leaving the system in an excited charge state with energy of order E_C. One option to go back to the charge ground state is given by a trivial reverse tunneling event along the same link which only adds an irrelevant additive constant to the effective low-energy code Hamiltonian. Dropping such constants, the leading-order process for relaxing back to the charge ground state comes from ring exchange along the elementary plaquettes involving four MCBs. The integration over the transient times of order E_C^{-1} where the system is virtually excited is most conveniently done by applying a Schrieffer-Wolff transformation [59]. We then obtain the effective low-energy code Hamiltonian [12]

$$H_{\rm code} = -\sum_n \text{Re}(c_n)\hat{\mathcal{O}}_n, \quad c_n = \frac{5}{16E_C^3}\prod t_{l_n l'_n}, \tag{5}$$

where n runs over all elementary plaquettes of the 2D network. Ignoring the code boundaries for the moment, this defines stabilizer operators $\hat{\mathcal{O}}_n$ as products of the eight Majorana operators comprising a minimal loop, $\hat{\mathcal{O}}_n = \prod_{j=1}^8 \gamma_j^{(n)}$. The

coefficients c_n in Eq. (5) involve the product of the four tunnel amplitudes around this loop. Note that the fluctuating phases φ_l have dropped out of Eq. (5) due to the Schrieffer-Wolff projection to the charge ground state of each MCB. A key feature of the Hamiltonian (5) is that all contributing operators commute, $[\hat{\mathcal{O}}_n,\hat{\mathcal{O}}_{n'}]=0$, since two plaquettes either share two or no Majorana operators. Each stabilizer operator is Hermitian, $\hat{\mathcal{O}}_n=\hat{\mathcal{O}}_n^\dagger$, and squares to unity, $\hat{\mathcal{O}}_n^2=1$. The Hilbert spaces defined by the two possible eigenvalues ±1 then correspond to the simultaneously measurable physical qubits of the Majorana surface code.

It is well known that interacting Majorana plaquette models as given in Eq. (5) can be mapped to (planar versions of) Kitaev's celebrated toric code model [18,19,60,61], which features long-range entanglement and topological order. In fact, our perturbative construction of Eq. (5) directly mirrors Kitaev's original derivation of the toric code from a strongly anisotropic variant of his honeycomb model [62], cf. Ref. [18]. We note that Refs. [63–67] discuss similar interacting Majorana networks which may yield alternative code constructions that differ from a surface code.

The mapping to the toric code also confirms that stabilizers must come in two different types, $\hat{\mathcal{O}}_n=\hat{X}$ or $\hat{\mathcal{O}}_n=\hat{Z}$, see Fig. 1. Indeed, by using the MCB Pauli operators $(\hat{x},\hat{y},\hat{z})_l$ introduced above, we observe that, away from lattice boundaries, every $\hat{X}$ ($\hat{Z}$) stabilizer operator is equivalently expressed as product of the four $\hat{x}$ ($\hat{z}$) Pauli operators on the adjacent MCBs numbered by $l_1\cdots l_4$ ($l_1'\cdots l_4'$),

$$\hat{X}=\hat{x}_{l_1}\hat{x}_{l_2}\hat{x}_{l_3}\hat{x}_{l_4},\quad \hat{Z}=\hat{z}_{l_1'}\hat{z}_{l_2'}\hat{z}_{l_3'}\hat{z}_{l_4'}. \tag{6}$$

The product is thus taken along the minimal path surrounding the respective plaquette. Again in agreement with the planar toric code, stabilizers located at the boundaries of the system only involve three Pauli (six Majorana) operators, see Fig. 1. It is worth noting that one could also take the fermion parity operators $\hat{\mathcal{P}}_l$, defined as the product of the four Majorana operators on MCB l, as a third type of stabilizer. This fact suggests the possibility of a Majorana surface code equipped with three different types of stabilizers $(\hat{X},\hat{Z},\hat{\mathcal{P}})$, cf. Refs. [19,20]. Under strong Coulomb blockade conditions, however, the parity constraint (1) locks all $\hat{\mathcal{P}}_l$ stabilizers into specific eigenstates. In what follows, we therefore employ only the $(\hat{X},\hat{Z})$-type stabilizers as active physical qubits.

In contrast to the commonly studied toric code model with just two couplings [62], we observe that the coupling constants $\mathrm{Re}(c_n)$ in Eq. (5) may effectively assume random values due to, e.g., the presence of tunnel phases or device imperfections. The temporal evolution of the system thus contains a large number of uncorrelated random phases $\exp[\pm i\mathrm{Re}(c_n)t]$ which lead to dephasing between corresponding stabilizer states with eigenvalues ±1. Protection of logical qubits against such dephasing processes forms an essential part of QIP with the surface code and can be effected, e.g., by reducing the respective $t_{ll'}$ couplings through gate voltage changes, see Sec. III A below. Errors could also arise from higher-order corrections to the code Hamiltonian in Eq. (5). For $|t_{ll'}|\ll E_C$, however, all sub-leading contributions beyond Eq. (5) are suppressed by at least a factor $(|t_{ll'}|/E_C)^2$. Such terms are not expected to seriously deteriorate the operation of the code. In any case, they can be handled in error correction along with the aforementioned and other (more severe) error sources, see Sec. IV F.

We conclude that the spin-1/2 variables represented by the MCB Pauli operators (2) constitute the elementary hardware qubits in our setup. Their definition is linked to the existence of topologically protected Majorana states. We therefore expect that these qubits come with long coherence times and thus represent attractive platforms for QIP operations in general [57]. Physical qubits (stabilizers) are then defined as products of four MCB Pauli operators along the minimal loops of the 2D lattice, see Eq. (6). For the definition of logical qubits, see Sec. III below.

C. Access hardware

Before moving on to the discussion of code operations, we introduce the hardware elements needed for initialization, manipulation, and readout of qubits. In particular, we will describe the implementation of tunnel conductance probes (including interference links), single-electron pumping, and the use of gate voltages. None of these elements involves the application of radiation fields. All access operations should be performed in the quasiadiabatic limit, i.e., at frequency scales well below the thresholds where radiation might be produced. The above elements could be integrated directly within the 2D code structure and do not require device technology beyond that needed to build the code itself. In view of the simplicity and flexibility of this architecture, alternative readout and/or manipulation schemes may also be implemented in an efficient manner, see Sec. IV F and Refs. [19,57].

1. Tunnel conductance probes

We consider all Majorana states to be endowed with tunable tunnel connectors to external probe leads. The presence of a weak tunnel coupling λ_l between a specific Majorana fermion γ_l and the lead fermion Ψ_l (near the corresponding tunnel contact) will be described by a tunneling operator, see Eq. (3) with $\Psi\to\Psi_l$, $\gamma_j\to\gamma_l$, $\hat{\varphi}\to\hat{\varphi}_l$, and $t_j\to\lambda_l$. These connections are essential for two-terminal interferometric transport measurements, which are our designated readout instrument for stabilizers, as well as for nonstabilizers like the MCB Pauli operators (2). For the latter type of readout, we need a tunnel link locally connecting the respective pair of leads. Such links allow for additional interference terms in the conductance which are sensitive to nonstabilizer eigenvalues, see below and Sec. IV A.

We first describe the measurement and readout of stabilizer eigenvalues. To that end, consider two neighboring Majorana states on adjacent MCBs, say, γ_0 and γ_1 in Fig. 1, which are connected by the effective tunnel matrix element t_{01}. Both Majorana states are also tunnel-coupled to separate probe leads. The application of a small bias voltage between these leads generates current flow, and the corresponding linear conductance, G_{01}, can be computed from an effective transfer Hamiltonian H_{01}. The latter follows by lowest-order expansion in $\lambda_{0,1}$, where we also perform a Schrieffer-Wolff transformation in order to project to the charge ground state on

each MCB, similarly to the steps leading to Eq. (5). We obtain

$$H_{01} = \alpha(\xi + c_u^* \hat{\mathcal{O}}_u + c_d \hat{\mathcal{O}}_d)\Psi_0^\dagger \Psi_1 + \text{H.c.}, \tag{7}$$

with $\alpha = -32\lambda_0\lambda_1^*/(5t_{01}^* E_C)$. Equation (7) features a superposition of a constant term (ξ), describing tunneling via the direct link $\sim t_{01}$, with two subleading terms of tunneling around nearby loops. The latter involve the Majorana strings $\hat{\mathcal{O}}_{u/d}$ around the upper (u) and lower (d) plaquette adjacent to the contacted pair $\gamma_0\gamma_1$, with the coefficients $c_{u,d}$ in Eq. (5). We find $\xi = (5/16)\eta|t_{01}|^2/E_C$ with a dimensionless asymmetry parameter $\eta \sim \Delta n_{g,0}\Delta n_{g,1} + \mathcal{O}(\Delta n_g^4)$; the full expression for η can be found in Ref. [12]. Importantly, η depends on detuning parameters $\Delta n_{g,l=0,1}$ off the respective particle-hole symmetric point (with integer $n_{g,l}$) at which the addition/removal of one charge unit to/from the MCB costs precisely the same energy (E_C). If at least one detuning vanishes, then the term $\sim\xi$ will be absent in Eq. (7). This cancellation of the direct process can be traced back to a destructive interference between different time-orderings of tunneling events. By varying the backgate voltage parameters $n_{g,l}$, one can then optimize the amplitude of the interference signal between the direct path and the loop contributions in the conductance readout below.

With the normal density of states $\nu_{l=0,1}$ of the respective probe lead, second-order perturbation theory in H_{01}, see Eq. (7), yields the tunneling conductance

$$\frac{G_{01}}{e^2/h} = 4\pi^2\nu_0\nu_1|\alpha|^2(g + g_u\mathcal{O}_u + g_d\mathcal{O}_d + g_{ud}\mathcal{O}_u\mathcal{O}_d). \tag{8}$$

Evidently, the conductance is sensitive to the stabilizer eigenvalues $\mathcal{O}_{u,d} = \pm 1$, where we tacitly assume that the conductance measurement implies a projection to the corresponding eigenstates, cf. Refs. [55,56]. Apart from a stabilizer-independent contribution with $g = \xi^2 + |c_u|^2 + |c_d|^2$, the conductance (8) contains quantum interference terms between the direct link and individual loops, $g_{u/d} = 2\xi\text{Re}(c_{u/d})$, and a two-loop interference term with $g_{ud} = 2\text{Re}(c_u c_d)$.

The coefficients (g, g_u, g_d, g_{ud}) will show random variations between readout configurations $(\gamma_l, \gamma_{l'})$ targeting different pairs of stabilizers. However, for a given pair, they are presumably time independent and can be parametrically altered by variation of the backgate parameters $n_{g,l/l'}$ and/or tunnel couplings $t_{ll'}$. Numerical values for these coefficients can be obtained by conductance measurements for the four different plaquette configurations $(\mathcal{O}_u, \mathcal{O}_d) = (\pm 1, \pm 1)$, where we anticipate that plaquettes can be flipped in a controlled manner by pumping protocols. Once the coefficients $\{(g, g_u, g_d, g_{ud})_{ll'}\}$ have been determined for all neighbor pairs by this initial calibration procedure, performing a (sequential or parallelized) measurement of the conductances along a set of $\approx N$ links (for a code with N MCBs) will determine all stabilizer eigenvalues.

Next we discuss the projective measurement and readout of nonstabilizer operators. These basal quantum operations will be extended to logical qubits in Sec. IV A, while here we introduce the needed hardware elements and conductance interferometry principles. For concreteness, we consider the Pauli operator $\hat{z} = i\gamma_5\gamma_6$ in Fig. 1, with eigenvalues $z = \pm 1$, where a suitably designed interferometric conductance measurement will be sensitive to this eigenvalue, see Eq. (10) below. In order to perform such a measurement, one can use the external leads already needed for stabilizer readout. In addition, we now require an interference link locally connecting both leads (away from MCBs) through a tunnel matrix element τ. To lowest order in the tunnel couplings $\lambda_{5,6}$, transport between both terminals is again governed by a transfer Hamiltonian (H_{56}). Repeating the steps leading to Eq. (7), we now obtain

$$H_{56} = (\tau + t_z\hat{z})\Psi_5^\dagger\Psi_6 + \text{H.c.} \tag{9}$$

with $t_z \sim \lambda_5\lambda_6^*/E_C$. The two-terminal conductance follows from perturbation theory as in Eq. (8),

$$\frac{G_{56}}{e^2/h} = 4\pi^2\nu_5\nu_6[|\tau|^2 + |t_z|^2 + 2\text{Re}(\tau^* t_z)z]. \tag{10}$$

After an initial calibration step, a conductance measurement thus determines z, where the measurement again implies a projection to the respective eigenstate of $\hat{z}$. We note that the amplitude of the interference signal can be optimized by tuning the link parameter τ. By using different lead pairs attached to the same MCB, one may access all Pauli operators ($\hat{x}$, $\hat{y}$, and $\hat{z}$) on this box. Similarly, for leads coupled to different MCBs, readout of other nonstabilizer operators (e.g., the string operators below) is possible, cf. Sec. IV A.

Finally, let us comment on the importance of higher-order corrections in tunnel couplings to the tunneling Hamiltonian(s) and to the conductance. If only the intercode couplings $t_{ll'}$ contributing to the target loop and to additional to-be-measured stabilizers are switched on during readout, e.g., $\mathcal{O}_{u,d}$ in Eq. (9), higher-order terms can only renormalize the transfer amplitudes, e.g., the couplings $\sim\xi, c_{u,d}$, and/or result in additional subleading terms with an operator content that is equivalent to the target loop up to stabilizer operators. Otherwise, they will not change the effective Hamiltonian describing transfer processes through the code. For instance, consider the two (wanted) loop processes around the stabilizers $\mathcal{O}_{u,d}$, which add to the direct lower-order (in $t_{ll'}$) contribution $\sim\xi$ in Eqs. (7) and (8). For readout of these stabilizers, such higher-order contributions will at worst make the identification between conductance outcomes and the corresponding stabilizer configurations slightly more involved. (Further aspects of higher-order loop contributions are discussed in terms of the charge pumping protocols in the next subsection.) Similarly, increasing the coupling strengths λ_l between code and external probe contacts does not affect the outcome of readout operations or manipulations, so long as afterwards the participating MCBs are relaxed to their respective charge ground states. In conclusion, the above readout mechanisms should also work when the $t_{ll'}$ or λ_l are tunable and, for manipulation purposes, operated outside of the deep tunneling regime. In either case, it is clear from the topology of the MCB network and the tunnel connections which operators might be addressed with a specific choice of probe or quantum dot contact points.

2. *Single-electron pumping*

Whereas conductance interferometry is our proposed readout tool, adiabatic charge pumping of single electrons onto and off the code by means of tunnel-coupled quantum dots will be tailor made for the controlled manipulation of qubits. For

simplicity, we assume that each quantum dot can accommodate only a single electron (occupation number $n = 0,1$), where the level energy is gate tunable. When the tunnel coupling $\tilde{\lambda}_l$ to the corresponding Majorana state γ_l is finite, by a suitable gate voltage change, one can pump (or absorb) one elementary charge into (from) the code [33,34]. The tunneling Hamiltonian is given by Eq. (3) with $\gamma_j \to \gamma_l$, $t_j \to \tilde{\lambda}_l$, $\hat{\varphi} \to \hat{\varphi}_l$, and $\Psi^\dagger \to d_l^\dagger$, where $d_l^\dagger$ is the fermion operator for the dot. Clearly, a single tunneling event will drive the respective MCB outside its charge ground state, and dot operations categorically have to be performed in pairs to maintain charge neutrality of the code. We here assume that the pumping operation is performed in an adiabatically slow way, at rates to be studied momentarily, although weak deviations from adiabaticity are not detrimental if combined with a measurement of the final dot occupations. Such control measurements collapse the system of dots into a definite state, thus eliminating diabatic errors that could spoil the code operation [68].

Denoting the initial charge configuration of the dot pair by $(n_l,n_{l'}) = (1,0)$, consider a gate-voltage protocol resulting in the final state (0,1). This process transfers precisely one electron through the code, entering via the Majorana state γ_l and exiting via $\gamma_{l'}$. The transfer Hamiltonian $H_{ll'}$ describing this process can be obtained by similar steps as those leading to Eq. (7) above, where we find

$$H_{ll'} = \mathcal{T}_{ll'} d_l \hat{\mathcal{S}}_{ll'} d_{l'}^\dagger, \quad \mathcal{T}_{ll'} \simeq \frac{\tilde{\lambda}_l^* \tilde{\lambda}_{l'}}{E_C} \prod_{j=1}^{m} \frac{t_{l_j l'_j}^*}{E_C}. \tag{11}$$

The transfer amplitude $\mathcal{T}_{ll'}$ has been specified up to a prefactor of no interest here, and $\hat{\mathcal{S}}_{ll'}$ represents string operators describing intracode electron transfer processes. In general, Eq. (11) involves a linear superposition of many contributions from different tunneling paths $\gamma_l \to \gamma_{l'}$ between the selected end-point Majorana states. For an arbitrary path with m tunneling events between neighboring MCBs ($\gamma_{l_j} \to \gamma_{l'_j}$ with tunnel links $j = 1,\ldots,m$), the string operator is given by the product of these $2m$ Majorana operators in addition to the end-point Majorana states [69],

$$\hat{\mathcal{S}}_{ll'} = (i\gamma_l \gamma_{l'}) \hat{W}_{ll'}, \quad \hat{W}_{ll'} = \prod_{j=1}^{m} \left(i\gamma_{l_j} \gamma_{l'_j}\right). \tag{12}$$

For $|t_{l_j l'_j}| \ll E_C$, the dominant term in Eq. (11) comes from the shortest path(s) with minimal number m of tunnel bridges. To give an example, for neighboring MCBs, we have $m = 1$ and the leading contribution takes the form $\hat{W}_{ll'} = i\gamma_{l_1}\gamma_{l'_1}$. When γ_l (and/or $\gamma_{l'}$) coincides with a Majorana operator in a given path $\hat{W}_{ll'}$, the destructive interference mechanism described above for the stabilizer readout configuration in Eq. (7) is activated. The path contribution to Eq. (11) can then be quenched by tuning the backgate parameter n_g (n'_g) on MCB l (l') to an integer value.

Since $\hat{W}_{ll'}$ in Eq. (12) stems only from intracode tunneling processes $\sim\gamma_{l_j}\gamma_{l'_j}$ between neighboring MCBs, such operators commute with all stabilizers, $[\hat{W}_{ll'},\hat{\mathcal{O}}_n] = 0$. This also implies that any two string operators $\hat{\mathcal{S}}_{ll'}$ are equivalent up to (products of) stabilizer operators. In a stabilized code state, the full operator content of the pumping process is therefore identified by the terminal Majorana operators. In fact, the two stabilizer operators $\hat{\mathcal{O}}_n$ containing γ_l are flipped by the above pumping protocol, since γ_l anticommutes with those two operators but commutes with all others. Similarly, the two stabilizers that contain $\gamma_{l'}$ will be flipped. It is then clear that, depending on the distance between γ_l and $\gamma_{l'}$, by such a charge transfer process one can flip zero, two, or four stabilizers. The case of no stabilizer flips corresponds to the above stabilizer readout scheme, see Eq. (7). In accordance with the planar toric code rules [62], stabilizers of each type thus can only be flipped in pairs. For instance, by pumping a single electron from $\gamma_7 \to \gamma_8$ in Fig. 1, the two adjacent $\hat{Z}$ plaquettes will be flipped. Since both γ_7 and γ_8 belong to the $\hat{X}$ plaquette in between, this stabilizer is flipped twice and hence remains invariant. We note that each string operator (12) can alternatively be written as product of MCB Pauli operators along a path from γ_l to $\gamma_{l'}$. In particular, for the above pumping process, $\hat{\mathcal{S}} = i\gamma_7\gamma_8 = \hat{x}$ connects the two flipped $\hat{Z}$ stabilizers in Fig. 1.

A single-electron pumping process can be considered adiabatic if it occurs on times scales long against $\tau_{\rm ad}$, where the energy scale $\tau_{\rm ad}^{-1} = |\mathcal{T}_{ll'}|$ corresponds to the leading-order contribution to $H_{ll'}$. Under these circumstances, the process will adiabatically transform an initial state $|\Psi\rangle_{\rm initial}$ into the final state $|\Psi\rangle_{\rm final} \sim \hat{\mathcal{S}}_{ll'}|\Psi\rangle_{\rm initial}$. We observe that when both dots are tunnel coupled to Majorana states on the same box, the pumping protocol implements elementary Pauli operations, cf. Eq. (2). In Sec. IV E, we will discuss powerful generalizations of the above protocols.

3. *Gate voltage adjustments*

The application of a static voltage to electrodes in spatial proximity of code elements can be used to adjust several important parameters of the code. For instance, by tuning the MCB backgate parameters $n_{g,l}$, one can alter the strength of path contributions to electron tunneling and optimize the interference signal for stabilizer readout operations. Similarly, by changing the voltage on gates near the tunnel bridges connecting neighboring MCBs, we may control the matrix elements $t_{ll'}$. For example, a minimal hole can be cut into the code by severing the four connections of a single stabilizer loop.

III. LOGICAL QUBIT IMPLEMENTATION

In Kitaev's original work on the toric code [62], a stabilizer system wrapped onto a surface of toroidal geometry was shown to exhibit topological ground-state degeneracy 2^{2g}, where g is the genus of the surface. The number $2g$ thus counts the unconstrained binary degrees of freedom. In principle, the latter are good candidates for topologically protected logical qubits due to their encoding into a stabilized code space. However, toroidal surfaces are difficult to realize in terms of 2D device technology, and the resulting qubits are almost impossible to address and/or read out. Later, it was realized that the torus topology can be effectively simulated in terms of a planar geometry [2,3], thereby paving the way for the surface code approach.

A simple example for a planar code patch with boundaries suitable to the definition of logical qubits is shown for our

architecture in Fig. 1. The shunting of Majorana states defines Z-type (or X-type) boundaries, where only $\hat{Z}$ (or $\hat{X}$) stabilizers appear at the respective boundary. The ground state, $|\Psi\rangle$, of the code Hamiltonian (5) has to satisfy the conditions $\hat{\mathcal{O}}_n|\Psi\rangle = \mathcal{O}_n|\Psi\rangle$ with eigenvalues $\mathcal{O}_n = \mathrm{sgn}[\mathrm{Re}(c_n)]$. However, these conditions are not sufficient to uniquely determine $|\Psi\rangle$. This can be seen by comparing the number of constraints (given by the number of stabilizers: 17 in Fig. 1) to the number of independent hardware qubits (MCBs: 18 in Fig. 1). We conclude that for the example in Fig. 1, one unconstrained degree of freedom remains. It corresponds to Pauli operators $\hat{Z}_{\mathrm{topo}}$ ($\hat{X}_{\mathrm{topo}}$) defined as product of all $\hat{z}$ ($\hat{x}$) MCB Pauli matrices along an arbitrary path connecting the two Z-type (X-type) code boundaries. Albeit $(\hat{Z}_{\mathrm{topo}}, \hat{X}_{\mathrm{topo}})$ encodes a logical qubit, this option is not very interesting since it just yields a single qubit, independent of the size of the code patch.

The ground-state degeneracy of such surface codes can be effectively enhanced by the controlled creation of holes, i.e., by excluding individual stabilizers from the readout operation applied to the majority of physical qubits in each computation cycle. We anticipate that such a procedure will represent a trade-off game, since for a dense pattern of holes, erroneous flips of the encoded logical qubits will become likely. We here introduce logical qubits in analogy to their definition in the bosonic surface code approach by Fowler *et al.* [10]. However, our Majorana surface code architecture comes with two differences of central importance.

First, Fowler *et al.* employ ancilla qubits (called measurement qubits in Ref. [10]) in addition to the physical qubits (data qubits in Ref. [10]). By entangling four data qubits with a measurement qubit through a sequence of controlled-NOT (CNOT) operations, projective stabilizer readout becomes possible. In our case, since readout is performed by conductance measurements using interference loops, see Sec. II C, neither measurement qubits nor additional CNOT operations are necessary. Compared to the bosonic variant, the present Majorana code architecture thus offers a significant reduction of hardware overhead together with a simpler single-step stabilizer measurement, see also Ref. [19].

Second, Fowler *et al.* implement a logical qubit as software hole by stopping certain CNOT operations between measurement and data qubits [10]. Since our Majorana code realization does not contain measurement qubits, we here need to proceed in a different manner. In order to exclude a stabilizer from the cyclic readout procedure, the gate-tunable tunnel couplings $\lambda_{l/l'}$ between the code and the respective leads, cf. Sec. II C, have to remain turned off. We note that it is not sufficient to simply switch off the respective bias voltage in the idle state since unbiased leads can, e.g., decohere the system. This procedure gives a software hole but not yet defines a useful logical qubit, since the two qubit eigenstates should be (nearly) degenerate to avoid large dephasing errors, cf. Sec. II B. To achieve this goal, we need a combined software-hardware hole, where also the intracode tunnel couplings $t_{ll'}$ are reduced by suitable gate voltage changes along the loop around a chosen stabilizer. The respective plaquette energy $\mathrm{Re}(c_n)$ in Eq. (5) thus decreases and one physically cuts a hardware hole into the code. Residual small plaquette energies can be handled in error correction, and to measure adjacent stabilizers one can sequentially turn on selected couplings $t_{ll'}$ again.

As reviewed in Ref. [10], larger holes for implementing logical qubits may be formed by combining several (d) adjacent holes. (The number d is the so-called code distance in terms of physical qubits.) The fault-tolerance threshold theorem [11] states that as long as error probabilities for elementary quantum operations remain below a moderate threshold value of order $\approx 1\%$, logical error rates become exponentially small with increasing d. This exponential scaling justifies the notion of topologically protected logical qubits [11]. In what follows, we mostly describe the case $d = 1$, with the understanding that a highly efficient reduction of logical errors is offered by increasing d. All operations are implemented such that they directly can be adapted to the case $d > 1$.

A. Single-cut qubits

Let us start with the most elementary logical qubit realizable in our code architecture, where one forms a hole for just a single plaquette. According to the above discussion, the removal of the corresponding constraint on $|\Psi\rangle$ leaves one binary degree of freedom undetermined. Since we have Z- and X-type stabilizers, two different types of logical qubits are possible, and by not measuring $\hat{Z}$ (or $\hat{X}$) we obtain a Z-cut (or X-cut) qubit, respectively. Suppose now that we have chosen a stabilizer, say, $\hat{Z}_1$ in Fig. 2. By convention, we take the Pauli-Z operator for this Z-cut qubit as the stabilizer operator $\hat{Z}_1$ itself. However, to define a logical qubit, we also need to identify the conjugate Pauli operator $\hat{X}_1$ anticommuting with $\hat{Z}_1$. This operator should not lead out of the code space spanned by simultaneous eigenstates of all other stabilizers. Obviously, once $\hat{X}_1$ has been constructed, the Pauli-Y operator will also be available by virtue of the relation $\hat{Z}_1\hat{X}_1 = i\hat{Y}_1$. Below we use the shorthand notation $(\hat{Z}_1, \hat{X}_1)$ for the resulting single-cut logical qubit.

An operator $\hat{X}_1$ with the required features can be constructed as product of all MCB Pauli-$\hat{x}$ operators connecting the internal X-type boundary around the open $\hat{Z}_1$ plaquette to an X-type code boundary along an arbitrary path, see Fig. 2. Note that this construction gives $\hat{X}_1$ as a string operator which trivially commutes with all X-type stabilizers but also with all other $\hat{Z}$ stabilizers (apart from $\hat{Z}_1$). The latter fact follows because $\hat{X}_1$ contains an even number (zero or two) of $\hat{x}$ operators that are conjugate to the $\hat{z}$ operators appearing in a given $\hat{Z}$. The only stabilizer affected by the string will be $\hat{Z}_1$, with anticommutator $\{\hat{X}_1, \hat{Z}_1\} = 0$, because the terminal Pauli-$\hat{x}$ operator present in $\hat{X}_1$ anticommutes with precisely one $\hat{z}$ in $\hat{Z}_1$. Alternatively, switching from the spin-1/2 to the Majorana language, one can understand the above properties by noting that $\hat{X}_1$ shares a single Majorana operator with $\hat{Z}_1$ but an even number of Majoranas with all other stabilizers of the code.

Summarizing, the two operators $(\hat{Z}_1, \hat{X}_1)$ define a logical qubit embedded into the code space of the system. An X-cut qubit may be defined analogously by ceasing the measurement of an X-type stabilizer, say, $\hat{X}_2$ in Fig. 2. With the conjugate Pauli operator $\hat{Z}_2$, which connects the $\hat{X}_2$-plaquette to a Z-type boundary via a string of $\hat{z}$ operators, we arrive at the logical qubit $(\hat{X}_2, \hat{Z}_2)$.

We emphasize that the definition of the string operators $\hat{X}_1$ and $\hat{Z}_2$ is not unique. For instance, instead of $\hat{Z}_2$, equivalent

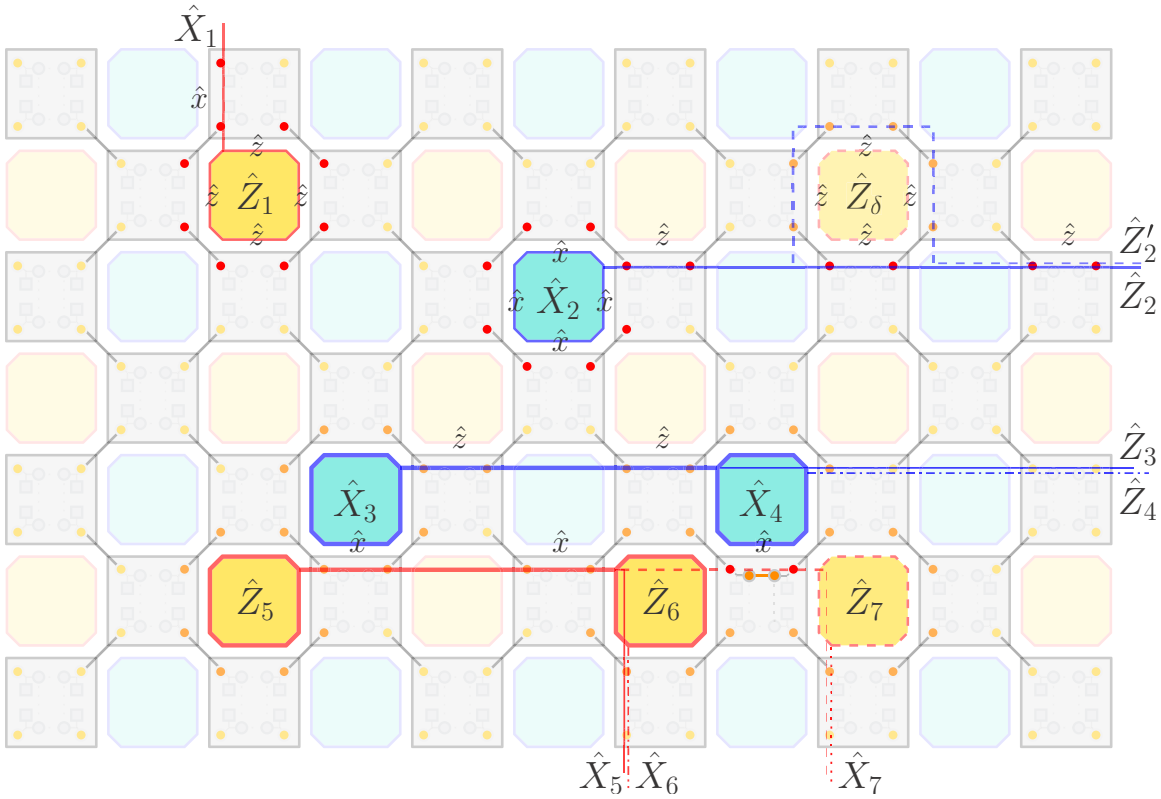

FIG. 2. Logical qubits in the Majorana code architecture (only a part of a larger 2D code is shown). By ceasing to measure the stabilizer $\hat{Z}_1$ (yellow, top left corner), one obtains the Z-cut qubit $(\hat{Z}_1, \hat{X}_1)$. The Pauli-$\hat{X}_1$ string connects $\hat{Z}_1$ to an X-type boundary (one choice is shown as red line). Similarly, $(\hat{X}_2, \hat{Z}_2)$ is an X-cut qubit, where we stop measuring $\hat{X}_2$ (dark blue). The string operator $\hat{Z}_2$ (blue line) connects $\hat{X}_2$ to a Z-type boundary, where an alternative choice $\hat{Z}_2' = \hat{Z}_\delta \hat{Z}_2$ is shown as well. Next, the X-type double-cut qubit $(\hat{X}_A, \hat{Z}_A)$ is built from two single-cut qubits $(\hat{X}_3, \hat{Z}_3)$ and $(\hat{X}_4, \hat{Z}_4)$. We use $\hat{X}_A = \hat{X}_3$ and the string operator $\hat{Z}_A = \hat{Z}_3 \hat{Z}_4$ connecting $\hat{X}_3$ and $\hat{X}_4$. Similary, the Z-type double-cut qubit $(\hat{Z}_B, \hat{X}_B)$ is formed from $(\hat{Z}_5, \hat{X}_5)$ and $(\hat{Z}_6, \hat{X}_6)$. Choosing $\hat{Z}_B = \hat{Z}_5$, both plaquettes are connected by the internal string operator $\hat{X}_B = \hat{X}_5 \hat{X}_6$. Finally, by readout of the MCB Pauli-$\hat{x}$ operator connecting $\hat{Z}_6$ and $\hat{Z}_7$ (probe leads shown as orange circles), logical information can be moved from $\hat{Z}_6 \to \hat{Z}_7$, i.e., the double-cut qubit B is then encoded between stabilizers no. 5 and 7, see Sec. IV B.

choices can be written as $\hat{Z}_2' = \hat{Z}_\delta \hat{Z}_2$, differing from $\hat{Z}_2$ by an arbitrary product operator $\hat{Z}_\delta$ of Z-type stabilizers, see Fig. 2 for an example. However, in a stabilizer eigenstate of $\hat{Z}_\delta$, the difference between $\hat{Z}_2$ and $\hat{Z}_2'$ reduces to a known sign corresponding to the measurement outcome $Z_\delta = \pm 1$. The only nontrivially related string operators in a fully stabilized code are those extending from the selected plaquette to different code boundaries. In that case, $\hat{Z}_2$ and $\hat{Z}_2'$ differ by the string operator $\hat{Z}_{\text{topo}}$ defined above. Likewise, for the Z-cut qubit, the string operator $\hat{X}_1' = \hat{X}_\delta \hat{X}_1$ is then related to $\hat{X}_1$ via the operator $\hat{X}_\delta = \hat{X}_{\text{topo}}$. In a similar way, if a code patch contains multiple holes, string operators adopt definitions differing by the not-measured stabilizers, depending on which side they pass around the hole(s). This property will be used extensively below in our implementation of CNOT and/or phase gates.

B. Double-cut qubits

Next we discuss how to implement a double-cut (or internal) qubit. This type of qubit serves to disconnect logical information from the code boundary, such that all operations appear as for an infinite system. In order to obtain a double-cut qubit, two single-cut qubits may be stitched together. For instance, consider the two X-cut qubits $(\hat{X}_3, \hat{Z}_3)$ and $(\hat{X}_4, \hat{Z}_4)$ in Fig. 2. We use a redundant encoding scheme, where the two-qubit state always remains in the, say, even-parity subspace defined by $X_3 X_4 = +1$. Such a constraint can be imposed by initial preparation and then kept throughout the computation by employing only a subset of qubit operators as detailed below. The even subspace is spanned by $\{|++\rangle_{34}, |--\rangle_{34}\}$, where the first (second) quantum number in each ket refers to the eigenvalue $X_3 = \pm 1$ ($X_4 = \pm 1$) of the respective single-cut qubit. Eigenstates of Pauli-Z operators are here denoted by $\hat{Z}|0\rangle = +|0\rangle$ and $\hat{Z}|1\rangle = -|1\rangle$, while Pauli-$X$ eigenstates are written as $|\pm\rangle = (|0\rangle \pm |1\rangle)/\sqrt{2}$.

We next identify $|+\rangle_A = |++\rangle_{34}$ and $|-\rangle_A = |--\rangle_{34}$ as the basis states of an X-type double-cut qubit $(\hat{X}_A, \hat{Z}_A)$. To complete the definition of this qubit, we have to specify the anticommuting Pauli operators $\hat{X}_A$ and $\hat{Z}_A$. To that end, let us first observe that any measurement of $\hat{X}_3$ alone suffices to stabilize the code since $X_4 = X_3$ is then directly known as well. This fact suggests $\hat{X}_A = \hat{X}_3$ (or, equivalently, $\hat{X}_A = \hat{X}_4$) as convenient choice for the Pauli-X operator. One easily verifies that the above $|\pm\rangle_A$ states are directly eigenstates of $\hat{X}_A$ with eigenvalues $X_A = \pm 1$. The conjugate Pauli-Z operator can then be chosen as $\hat{Z}_A = \hat{Z}_3 \hat{Z}_4$, which anticommutes with $\hat{X}_A = \hat{X}_3$ (or $\hat{X}_4$) and gives $\hat{Z}_A |\pm\rangle_A = |\mp\rangle_A$. For plaquettes

$\hat{X}_3$ and $\hat{X}_4$ located away from the code boundaries (as in Fig. 2), $\hat{Z}_A$ can be represented by an internal string operator not involving boundary degrees of freedom. Indeed, all $\hat{z}$ operators appearing in the string $\hat{Z}_4$ will square to unity when combined with $\hat{z}$ operators from the same part of the path in $\hat{Z}_3$, see Fig. 2. In effect, only the $\hat{z}$ operators along the internal path connecting $\hat{X}_3$ and $\hat{X}_4$ will then contribute to $\hat{Z}_A$.

We conclude that an X-type double-cut qubit $(\hat{X}_A, \hat{Z}_A)$ can be obtained by the combination of two X-type single-cut qubits. We can thereby redundantly encode an arbitrary qubit state,

$$|\psi\rangle_A = \alpha|+\rangle_A + \beta|-\rangle_A, \tag{13}$$

with complex-valued coefficients α, β. In Sec. IV, we describe how such a state may be initialized, manipulated, and read out using the hardware elements introduced in Sec. II.

By following basically the same steps as just outlined, one can also implement a Z-type double-cut qubit. This is illustrated in Fig. 2 for the qubit $(\hat{Z}_B, \hat{X}_B)$ formed from the single-cut qubits corresponding to $\hat{Z}_5$ and $\hat{Z}_6$ (or $\hat{Z}_7$). Furthermore, completely analogous arguments apply to redundant encoding schemes using the odd subspace. The choice regarding which subspace is employed follows from the last stabilization cycle before a pair of stabilizers is left open to form the double-cut qubit. Since all proper double-cut operators work within this subspace, this qubit property will be kept throughout the computation (unless errors occur which need to be handled in error correction).

IV. BASAL QUANTUM LOGICAL OPERATIONS

So far, we have discussed the implementation of a physical qubit network and how logical qubits may be immersed into it. Starting from there, the realization of QIP will advance in three hierarchical stages. At the base level, we need protocols to manipulate logical information, that is, to initialize logical qubits, to change their state, to move and braid them, and to read them out. These basal operations are constructed from interferometric conductance measurements and/or electron pumping protocols, relying on the access hardware in Sec. II C. This will pave the way towards the second stage, the realization of a minimal set of logical gates for universal quantum computation. The third level implements algorithms and will not be discussed here.

It is important to realize that the required number of basal operations increases dramatically at each consecutive level. Let us briefly illustrate this point, where we also provide a short overview over this central section. First, given the capability to initialize and read out qubit states and/or string operators, see Sec. IV A, the movement of a logical qubit from one plaquette to an adjacent one will require interferometric readout, control measurements, and qubit flips depending on outcomes, see Sec. IV B. Second, the formation of the braid transformation, which is instrumental to the realization of the workhorse gate of most QIP operations, the CNOT, then requires several qubit moves, see Sec. IV C. Third, more complex operations in turn involve sequences of CNOT and/or Hadamard operations. Furthermore, the realization of phase gates hinges on the availability of ancilla states, where we propose the possibility to prepare Pauli eigenstates on a separate auxiliary system, followed by a state injection process transferring the state to a code qubit, see Sec. IV D. Next, in Sec. IV E, we show how to prepare and manipulate qubit states in terms of general electron pumping protocols. In Sec. IV F, we then offer a discussion of likely error sources and challenges in our code architecture. While a description of quantum error correction is beyond the scope of our work, we expect that (given this toolkit of basal operations) one can largely follow the surface code strategies reviewed in Refs. [10,11].

In view of this proliferation of complexity, maximum efficiency and reliability in these basal operations will be decisive for success. This is, we believe, where the present approach has great advantages to offer. The fact that qubit measurements and state changes are realized via relatively undemanding single-step operations as compared to, say, the five-step ancilla-state-based CNOT protocol proposed for bosonic codes [10], will have an exponential impact on the complexity of later design stages. Below we propose a set of basal QIP operations realizing the first development stage. With these operations in place, the implementation of all gates needed for universal quantum computation is possible as summarized in Sec. V. However, the essential novelties of our approach are contained in the present section.

A. Initialization and projective measurements

For the initialization of stabilizer eigenstates, we may simply take the last readout result. In case the string eigenstate of a double-cut qubit is needed, we can utilize interferometric conductance measurements of MCB Pauli operators, see below and Sec. II C. To that end, starting from a stabilized state, say, for qubit $(\hat{X}_A, \hat{Z}_A)$ in Fig. 2, one first measures all constituent Pauli-$\hat{z}$ operators contributing to the string operator $\hat{Z}_A$. The intermediately affected stabilizers outside of qubit A then re-enter the readout cycle, and the $\hat{Z}_A$-string eigenstate (identified by outcomes $z = \pm$) remains.

Various other operations also require the initialization/readout of MCB spin-1/2 states in definite Pauli ($\hat{x}$, $\hat{y}$, or $\hat{z}$) eigenstates and/or the projective measurement of short string operators. General string operators are written as a product of a few MCB Pauli (or twice as many Majorana) operators. Equivalently, they can be represented by (at most) two double-cut qubit string operators and, if multiple nonequivalent strings between two end points are used, a number of stabilizer operators of the surface code, cf. Secs. II C and III. The initialization (measurement) of MCB Pauli and/or string eigenstates (operators) can then be effected by conductance interferometry as described next.

First, a given MCB spin can be sent into a Pauli eigenstate by connecting a pair of leads (equipped with an interference link) to the two Majorana states corresponding to the Pauli operator in question, see Eq. (2). Figure 2 illustrates such a measurement for the Pauli-$\hat{x}$ operator connecting the stabilizers $\hat{Z}_6$ and $\hat{Z}_7$. The conductance then contains an interference contribution sensitive to the measured Pauli eigenvalue, see Eq. (10), and the measurement projects the system to the corresponding eigenstate. In case that the opposite eigenstate is needed, one can employ a single-electron pumping process (see Sec. II C) to flip to the other eigenvalue. Alternatively, if only so-called Clifford operations (mapping Pauli to Pauli operators) are

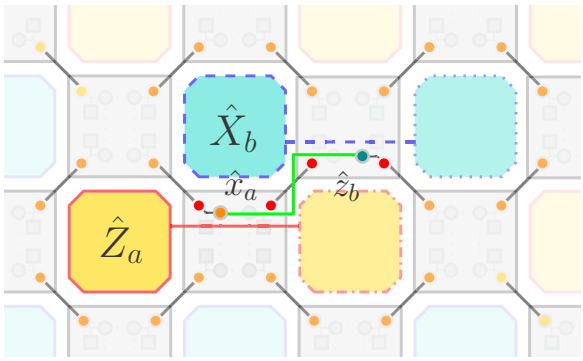

FIG. 3. Similar to Fig. 2 but illustrating string operator measurements, where $\hat{\mathcal{S}} = \hat{x}_a\hat{z}_b$ is measured by conductance interferometry using the marked leads (orange and blue circles) sharing an interference link (green). Noting the equivalent representation $\hat{\mathcal{S}} = \hat{X}_a\hat{Z}_b$, an arbitrary state $|\psi\rangle$ can be moved from the Z-type double-cut qubit $(\hat{Z}_a, \hat{X}_a)$ to the adjacent X-type qubit $(\hat{X}_b, \hat{Z}_b)$. An alternative approach employs the stabilizer product operator $\hat{\mathcal{M}} = \hat{Z}_a\hat{X}_b$, see the main text.

performed, such flips can be processed by classical software, see Ref. [10] for details.

Next we describe how to measure string operators. As a concrete example, an implementation of the Hadamard gate is possible by measuring the string operator $\hat{\mathcal{S}} = \hat{x}_a\hat{z}_b = \hat{X}_a\hat{Z}_b$ in Fig. 3, see Secs. IV B and V B below. Noting that $\hat{\mathcal{S}}$ affords an equivalent representation as a product of four Majorana operators, one can access $\hat{\mathcal{S}}$-eigenstates by activating the leads connected to the outermost of these four Majoranas, see Fig. 3. For leads sharing an interference link, in close analogy to Eq. (10), the conductance will then depend on the eigenvalue $\mathcal{S} = \pm 1$. This interferometric measurement also implies a projection to the corresponding string eigenstate.

An alternative measurement offering similar functionality can be employed for the stabilizer product operator $\hat{\mathcal{M}} = \hat{Z}_a\hat{X}_b$. To this end, one may activate the tunnel links surrounding $\hat{Z}_a$ and $\hat{X}_b$ in Fig. 3 while quenching the one shared by both stabilizers. Projection onto individual eigenstates is thus avoided, and an adjacent pair of leads in stabilizer readout configuration (cf. Sec. II C) may access $\mathcal{M} = \pm 1$. In this intracode interferometry approach, no interference links are required beyond those already needed for MCB Pauli operator readout.

B. Moving logical qubits

Any gate implementation involves the transfer of logical qubits, either as part of the process itself or to move information to some desired storage zone afterwards. In the following, we first discuss a single-cell shift where the target qubit is of the same type as the source qubit, followed by the description of how to perform a state transfer between adjacent qubits of different (Z/X) type. Extended motion paths can then be realized by iteration.

1. Same-type qubits

We start by describing the state transfer between two same-type qubits. For concreteness, let us consider the single-cut qubit $(\hat{Z}_6, \hat{X}_6)$ in Fig. 2, assumed to be prepared in an arbitrary state $|\psi\rangle$. We wish to move $|\psi\rangle$ from this source qubit a, with $\hat{Z}_a = \hat{Z}_6$, to the adjacent target qubit b, given by $(\hat{Z}_7, \hat{X}_7)$ in Fig. 2, with $\hat{Z}_b = \hat{Z}_7$. From the last stabilization cycle, the target qubit has been prepared in a known stabilizer state, say, the Pauli-Z eigenstate $|0\rangle_b$ with eigenvalue $Z_b = +1$. We thus start from the product initial state

$$|\Psi_0\rangle = |\psi\rangle_a \otimes |0\rangle_b = (\alpha|0\rangle + \beta|1\rangle)_a \otimes |0\rangle_b, \tag{14}$$

where all operations are designed such that only qubits explicitly addressed during the move are affected and all other physical qubit states can be factored out. When the move is completed, $\hat{Z}_a$ has become part of the stabilizer readout cycle, while $\hat{Z}_b$ is left open and then contains the state $|\psi\rangle$. We note that there is no need to specify where the string operators $\hat{X}_a$ and $\hat{X}_b$ terminate. In fact, our protocol will directly apply to a double-cut qubit, say, $(\hat{Z}_B, \hat{X}_B)$ in Fig. 2 with both strings ending at $\hat{Z}_5$.

In order to move the logical information, one needs to perform a projective measurement that entangles the source and target qubits. Such a measurement can be implemented by readout of the MCB Pauli operator $\hat{x}_{ab} = \hat{X}_a\hat{X}_b$, cf. also Fig. 2, which we have already described in Secs. II C and IV A. Note that $\hat{x}_{ab}$ is precisely the string operator connecting $\hat{Z}_a$ and $\hat{Z}_b$. Assuming the measurement outcome $x_{ab} = +1$, the state $|\Psi_1\rangle$ found after the readout is projected to the corresponding eigenstate of $\hat{x}_{ab}$. (For the other outcome $x_{ab} = -1$, see below.) Switching to the Pauli-X basis and taking into account $\langle\hat{X}_a\hat{X}_b\rangle = x_{ab} = +1$, we find the (not-normalized) state

$$|\Psi_1\rangle = (\alpha + \beta)|++\rangle_{ab} + (\alpha - \beta)|--\rangle_{ab}. \tag{15}$$

For generic α, β, this is an entangled state of the source and target qubits.

We now include $\hat{Z}_a$ in the next stabilizer readout cycle (assuming outcome $Z_a = +1$) but cease to measure $\hat{Z}_b$. Switching back to the Pauli-Z basis and projecting the source qubit to $|0\rangle_a$, we arrive at

$$|\Psi_2\rangle = |0\rangle_a \otimes (\alpha|0\rangle + \beta|1\rangle)_b = |0\rangle_a \otimes |\psi\rangle_b. \tag{16}$$

Evidently, we have achieved a perfect transfer of the state $|\psi\rangle$ from the source to the target qubit.

In the above discussion, we have made three assumptions about measurement outcomes, namely $Z_b = +1$ for the initial, $x_{ab} = +1$ for the intermediate, and $Z_a = +1$ for the final readout. However, different outcomes can be accomodated by applying suitable Pauli-flip operators to the target qubit. In particular, the state $|\Psi_2\rangle$ in Eq. (16) can be reconstructed from the bare final state $|\Psi_2\rangle_{\text{bare}}$ obtained from the above protocol,

$$|\Psi_2\rangle = (\hat{Z}_b)_{x_{ab}=-1}(\hat{X}_b)_{Z_aZ_b=-1}|\Psi_2\rangle_{\text{bare}}, \tag{17}$$

where the first (second) Pauli operator is only applied for $x_{ab} = -1$ (for $Z_aZ_b = -1$). For Clifford-only operations, as mentioned above, the Pauli flips in Eq. (17) can be taken into account by the classical software used for processing measurement outcomes. We conclude that this protocol for moving quantum information by one unit cell between same-type stabilizers can be employed for arbitrary outcomes.

As with any unitary quantum operation, such a qubit move affords either a Schrödinger interpretation, in which the state

changes as $|\psi\rangle_a \otimes |0\rangle_b \to |0\rangle_a \otimes |\psi\rangle_b$, or a Heisenberg view, in which states remain invariant but the logical qubit operators change as $(\hat{Z},\hat{X})_a \to (\hat{Z},\hat{X})_b$. The picture in which operators, rather than states, are subject to manipulation will often be more convenient in the description of logical qubit operations below.

2. *Different-type qubits*

Finally, by a modified version of the above protocol, we can also transfer a state $|\psi\rangle$ between different (Z/X) types of logical qubits, see Fig. 3. In that case, we start from an initial two-qubit state

$$|\Psi_0\rangle = (\alpha|0\rangle + \beta|1\rangle)_a \otimes |+\rangle_b = |\psi\rangle_a \otimes |+\rangle_b, \tag{18}$$

where the state $|\psi\rangle$ is stored on the Z-type qubit a, and the X-type target qubit b has been prepared in the $X_b = +$ eigenstate, see Fig. 3. Instead of a single MCB Pauli operator, in the present case we have to measure the string operator $\hat{\mathcal{S}} = \hat{x}_a\hat{z}_b$ in Fig. 3 in order to perform the move operation. Note that $\hat{\mathcal{S}}$ is equivalent to the product of the internal string operators of both qubits, $\hat{\mathcal{S}} = \hat{X}_a\hat{Z}_b$. This measurement can be done as described in Sec. IV A, and we momentarily assume the outcome $\mathcal{S} = +1$.

To show that the $\hat{\mathcal{S}}$-measurement indeed effects the state transfer from a to b, we observe that, in analogy to Eq. (15), the projection to $\mathcal{S} = +1$ yields the intermediate state

$$|\Psi_1\rangle = (\alpha+\beta)|+\rangle_a \otimes |0\rangle_b + (\alpha-\beta)|-\rangle_a \otimes |1\rangle_b. \tag{19}$$

Letting qubit a enter the stabilizer readout cycle and assuming the outcome $Z_a = +1$, we arrive at the final configuration

$$|\Psi_2\rangle = |0\rangle_a \otimes (\alpha|+\rangle + \beta|-\rangle)_b = |0\rangle_a \otimes (\hat{H}|\psi\rangle)_b. \tag{20}$$

Recalling that the Hadamard ($\hat{H}$) operation effectively exchanges $\hat{X}$ and $\hat{Z}$ operators [58], the final state of qubit b is interpreted as the target state of an $\hat{H}$ operation applied to the initial state $|\psi\rangle$ of qubit a. For other measurement outcomes, one again has to apply Pauli-flip operators (or classical postprocessing) to qubit b.

Finally, a variant of this protocol can be implemented by using the stabilizer product operator $\hat{\mathcal{M}} = \hat{Z}_a\hat{X}_b$. After initial preparation of a string eigenstate $Z_b = \pm 1$ and entangling qubits a and b via measurement of $\hat{\mathcal{M}}$, one then obtains the Hadamard-transformed state on qubit b by measurement of the string operator $\hat{X}_a$.

We conclude that the state $|\psi\rangle$ initially stored on the $\hat{Z}_a$ stabilizer of qubit a has been transferred to storage in the $\hat{X}_b$ stabilizer of qubit b. Since they are of different (Z/X) type, this transfer effects a Hadamard gate on the logical state, cf. Sec. V B below.

C. Braiding logical qubits

The motion of logical qubits leaves information unchanged unless the strings forming part of the construction of cut-qubits are crossed. By contrast, when moving one qubit around another one, such a crossing must necessarily occur. Using the same convention for string definitions (cf. Sec. III) before and after this qubit braid transformation, the crossing enforces a transformation of qubit operators equivalent to the fundamental CNOT operation, see below and Sec. V A. In the following we illustrate this concept for the basic braid operation of transferring a Z-type qubit around an X-type qubit.

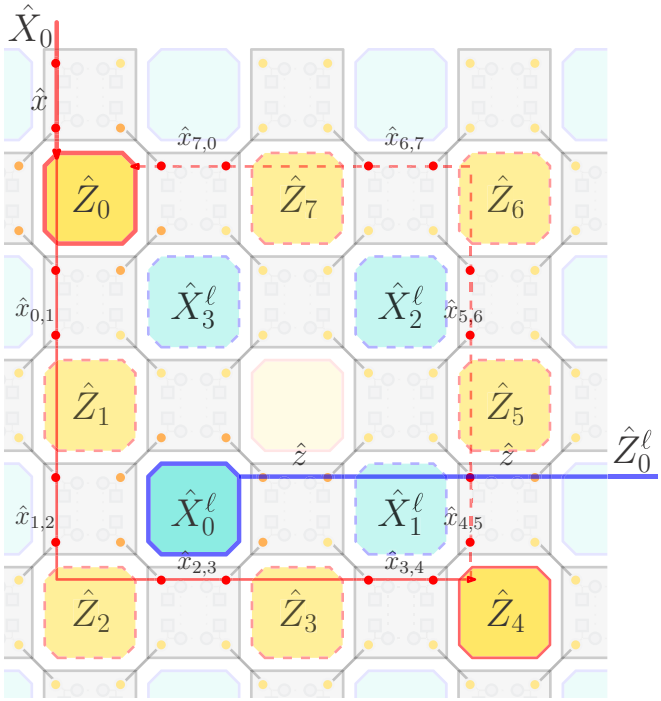

FIG. 4. Similar to Fig. 2 but now for a braid operation of logical qubits $(\hat{Z}_A,\hat{X}_A) = (\hat{Z}_0,\hat{X}_0)$ and $(\hat{X}_B,\hat{Z}_B) = (\hat{X}_0^\ell,\hat{Z}_0^\ell)$. The stabilizers $\hat{Z}_0$ (yellow) and $\hat{X}_0^\ell$ (blue) are highlighted, and a choice for the string operators $\hat{X}_0$ (thick red line) and $\hat{Z}_0^\ell$ (blue solid line) is shown. By iterating the single-step operations in Sec. IV B (or by analogous multi-step moves), qubit A is moved to $\hat{Z}_A = \hat{Z}_4$ and $\hat{X}_A = \hat{X}_4$. We then bring A back to the initial position by encircling B. After a full loop, one has crossed the string $\hat{Z}_B$. This braid transformation entangles both qubits according to Eq. (23) and thereby implements a CNOT gate.

To this end, consider $(\hat{Z}_A,\hat{X}_A)$ and $(\hat{X}_B,\hat{Z}_B)$ in Fig. 4 with the shown convention for string operators. We aim to move A along a closed loop encircling B. This operation affects B because, in the process, the $\hat{Z}_B$-string emanating from the $\hat{X}_B$ plaquette must be crossed, i.e., $(\hat{Z}_{A/B},\hat{X}_{A/B})_{\text{initial}} \to (\hat{Z}_{A/B},\hat{X}_{A/B})_{\text{final}}$ changes both qubits. To understand how, imagine $\hat{Z}_A$ moved along the loop in Fig. 4, for instance by a sequence of single-step movements as described in Sec. IV B. Up to a known sign, this brings $(\hat{Z}_A)_{\text{final}} = (\hat{Z}_A)_{\text{initial}}$ back to the original configuration. We stress that the same initial and final conventions are taken to define the string operators $\hat{X}_A$ and $\hat{Z}_B$, which escape directly towards the top and the right boundary in Fig. 4, respectively. The string operator $\hat{X}_A$ will then change as $(\hat{X}_A)_{\text{final}} = \hat{X}_{\text{loop}}(\hat{X}_A)_{\text{initial}}$, where the loop operator

$$\hat{X}_{\text{loop}} = \hat{x}_{0,1}\hat{x}_{1,2}\cdots\hat{x}_{7,0} \tag{21}$$

comprises the product of all MCB Pauli operators $\hat{x}_{l,l+1}$ adding to the string along its stepwise extension around the loop in Fig. 4.

The operator (21) affords the alternative representation

$$\hat{X}_{\text{loop}} = \hat{X}_0^\ell \hat{X}_1^\ell \hat{X}_2^\ell \hat{X}_3^\ell, \tag{22}$$

where $\hat{X}_j^\ell$ denotes the $\hat{X}$ operators tiling the area surrounded by the loop. The equivalence of both representations follows from the fact that of the 4×4 Pauli-$\hat{x}$ operators entering the product of $\hat{X}_j^\ell$ operators in Eq. (22), all those sitting on links in the bulk of the area will pairwise square out. The uncompensated $\hat{x}$ at the loop boundary are precisely those appearing in Eq. (21). Now, of the four $\hat{X}_j^\ell$ stabilizers appearing in the product (22), three are part of the readout cycle and thus only contribute a known sign to the result. The only exception is $\hat{X}_0^\ell = \hat{X}_B$, and (up to that sign) we arrive at $(\hat{X}_A)_{\text{final}} = (\hat{X}_B)_{\text{initial}}(\hat{X}_A)_{\text{initial}}$.

Finally, the change of $\hat{Z}_B$ follows from the interpretation in which the motion of A around B is viewed as one of B around A. This amounts to a crossing of the $\hat{Z}_B$ string with the $\hat{X}_A$ string, and by the argument above, we have $(\hat{Z}_B)_{\text{final}} = (\hat{Z}_A)_{\text{initial}}(\hat{Z}_B)_{\text{initial}}$. At the same time, $\hat{X}_B$ remains unchanged in the process, $(\hat{X}_B)_{\text{final}} = (\hat{X}_B)_{\text{initial}}$.

These braiding rules are summarized by the four basic transformation laws (with identity $\hat{I}$),

$$\begin{aligned} &\hat{Z}_A \otimes \hat{I}_B \to \hat{Z}_A \otimes \hat{I}_B, \quad \hat{I}_A \otimes \hat{Z}_B \to \hat{Z}_A \otimes \hat{Z}_B, \\ &\hat{X}_A \otimes \hat{I}_B \to \hat{X}_A \otimes \hat{X}_B, \quad \hat{I}_A \otimes \hat{X}_B \to \hat{I}_A \otimes \hat{X}_B. \end{aligned} \tag{23}$$

The braid operation is of paramount importance in that it implements the CNOT operation on the two qubits A and B, see Sec. V A.

D. State injection

It may often be convenient to initialize a state in a separate auxiliary system, where the state is subsequently injected into a target logical qubit near the boundary of the bulk surface code. A setup allowing for such a state injection process is shown in Fig. 5, where an auxiliary MCB with Pauli operators $(\hat{x}_a, \hat{y}_a, \hat{z}_a)$ is tunnel coupled to a MCB within the code but located at its boundary. This process can be particularly helpful for generating the ancilla states needed for phase gate implementations (see Sec. V) since the state preparation can be optimized on a separate device away from the code.

Initially, the auxiliary MCB a is assumed to be decoupled, i.e., tunnel couplings to the code are turned off. We then imagine preparing an arbitrary state $|\psi\rangle = \alpha|0\rangle + \beta|1\rangle$ on this MCB, without affecting the decoupled code state. For instance, Pauli eigenstates can be directly initialized as discussed in Sec. IV A. As target qubit, we consider the double-cut qubit $(\hat{Z}_b, \hat{X}_b)$ near the code boundary in Fig. 5. Assuming the initialization $Z_b = +$, we thus start from

$$|\Psi_0\rangle = |\psi\rangle_a \otimes |0\rangle_b. \tag{24}$$

We next switch on the tunnel couplings connecting MCB a to the code and cease to measure the two $\hat{Z}$-stabilizers defining the target qubit. To achieve the state transfer from a to b, we then perform a projective measurement of the operator $\hat{X}_* = \hat{X}_b \hat{x}_a$ (green square in Fig. 5), which anticommutes with both $\hat{Z}_b$ and $\hat{z}_a$. This can be done by conductance interferometry using a pair of leads attached to (say) the upper two Majorana states in the $\hat{X}_*$ loop, similarly to the stabilizer readout described in Sec. II C.

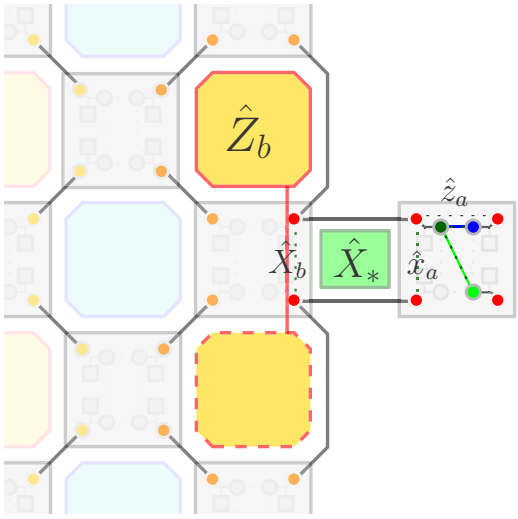

FIG. 5. Setup for state injection into the surface code. An auxiliary MCB with Pauli operators $(\hat{x}_a, \hat{y}_a, \hat{z}_a)$ is tunnel coupled to a MCB belonging to the code but located near a (Z-type) boundary. An arbitrary state $|\psi\rangle$ may now be prepared on the decoupled MCB a. Pauli eigenstates can be initialized by conductance interferometry, where the green dotted line indicates a lead pair (with interference link) for measuring $\hat{y}_a$. Subsequently connecting MCB a to the code, ring exchange processes identify the operator $\hat{X}_* = \hat{X}_b \hat{x}_a$ (green square), where $\hat{X}_b$ is the internal string operator for the double-cut code qubit $(\hat{Z}_b, \hat{X}_b)$. By measuring $\hat{X}_*$ via conductance interferometry, and finally disentangling MCB a from the code (by measurement of $\hat{z}_a$), $|\psi\rangle$ is transferred to the target qubit b.

We can verify the state transfer from MCB a to the code qubit b as follows. By writing $|\Psi_0\rangle$ in the Pauli-X basis for both qubits and then projecting to the $\hat{X}_*$ eigenstate with, say, $X_* = +$, we obtain the intermediate state

$$|\Psi_1\rangle = (\alpha + \beta)|++\rangle_{ab} + (\alpha - \beta)|--\rangle_{ab}. \tag{25}$$

We now disentangle both qubits by measuring $\hat{z}_a$ on MCB a via conductance interferometry. Assuming the outcome $z_a = +$, we arrive at the final state,

$$|\Psi_2\rangle = |0\rangle_a \otimes (\alpha|0\rangle_b + \beta|1\rangle_b) = |0\rangle_a \otimes |\psi\rangle_b. \tag{26}$$

For other outcomes, one may have to apply Pauli flip operators as described for a qubit move in Sec. IV B.

We have thereby injected an arbitrary ancilla state $|\psi\rangle$ from the auxiliary MCB (where it has been prepared) to a target qubit of the surface code. Another injection step can then take place as soon as the logical information on the target qubit has been transported away from the code boundary.

E. Multistep pumping protocols

A major challenge for any universal quantum computation scheme is to implement a non-Clifford gate such as the general phase gate $\hat{P}(\theta)$, where the single-qubit operator

$$\hat{P}(\theta) = e^{i\theta\hat{Z}} \tag{27}$$

performs a Bloch sphere rotation around the Z axis. In particular, the $\hat{T}$ gate (also called the $\pi/8$ gate) follows by choosing the phase angle $\theta = -\pi/8$ [58]. As discussed in

Sec. V D below, it may be advantageous to realize the phase gate operation on an arbitrary logical qubit state $|\psi\rangle$ by first generating ancilla states using $\hat{P}(\theta)$. Such a state can then be consumed in a quantum circuit that entangles the logical and ancilla qubits during intermediate steps of the protocol, where the (perfect copy of an) initial ancilla state is given by

$$|A_\theta\rangle = \hat{P}(\theta)|+\rangle = (e^{i\theta}|0\rangle + e^{-i\theta}|1\rangle)/\sqrt{2}. \quad (28)$$

For a successful phase gate implementation, we thus have to be able to accurately prepare this specific ancilla state. In what follows, we show that this task can be achieved in our code architecture by means of a four-step adiabatic electron pumping protocol. The latter can be experimentally realized by sweeping gate voltages on quantum dots which in turn are tunnel coupled to individual Majorana states, see Sec. II C.

As an ancilla qubit, we consider the Z-type double-cut qubit $(\hat{Z},\hat{X})$ in Fig. 6. By means of an interferometric measurement, see Sec. IV A, the qubit is assumed to be initially prepared in the $|+\rangle$ eigenstate of the internal string operator $\hat{X}$. We show below that the state $|A_\theta\rangle$ in Eq. (28) can then be generated by a multistep pumping protocol employing two pairs of single-level quantum dots denoted by (0,2) and (3,4) in Fig. 6. Each dot has a gate-tunable level energy ε_j and is attached to the respective Majorana operator γ_j (with $j = 0,2,3,4$). The system will be operated in a parameter regime where each dot pair holds a single electron. For simplicity, we consider antisymmetric energy configurations, where only the two energies $\varepsilon_{a/b}$ with

$$\varepsilon_a/2 = \varepsilon_0 = -\varepsilon_2, \quad \varepsilon_b/2 = \varepsilon_3 = -\varepsilon_4, \quad (29)$$

are changed during the protocol. With the large positive energy scale D, by slowly varying ε_a from $-D \to +D$ (or in reverse order $+D \to -D$), a single electron will be adiabatically pumped from dot $0 \to 2$ (or vice versa). By sweeping ε_b, we can similarly pump an electron between dots 3 and 4.

Let us first address the dot pair $a = (0,2)$ with fermion operators (d_0,d_2) subject to the condition $d_0^\dagger d_0 + d_2^\dagger d_2 = 1$. It is instructive to describe this dot pair by the equivalent spin-1/2 operator $\vec{S}_a = (S_a^x, S_a^y, S_a^z)$ with

$$S_a^z = \tfrac{1}{2}(d_0^\dagger d_0 - d_2^\dagger d_2), \quad S_a^+ = d_0^\dagger d_2, \quad S_a^- = (S_a^+)^\dagger, \quad (30)$$

where $S_a^\pm = S_a^x \pm i S_a^y$. We denote the eigenstate of S_a^z to eigenvalue $\pm 1/2$ as $|\uparrow/\downarrow\rangle_a$. The corresponding occupation number states on this dot pair are $|10\rangle_{02} = |\uparrow\rangle_a$ and $|01\rangle_{02} = |\downarrow\rangle_a$, see Fig. 6. By steps as detailed in Sec. II C, after a Schrieffer-Wolff projection to the charge ground state of the MCBs, transfer processes between dots (0,2) are then encoded by the effective spin-1/2 Hamiltonian

$$H_a = \varepsilon_a S_a^z + \hat{T}_a S_a^+ + \hat{T}_a^\dagger S_a^-, \quad \hat{T}_a = i t_a^x \hat{X} + t_a^y \hat{Y}. \quad (31)$$

The transfer operator $\hat{T}_a$ comes from summing over all possible tunneling paths through the code which connect the two dots. We here assume that physical qubits surrounding the double-cut qubit in Fig. 6 are either in a stabilized state or turned off (see Sec. II C). In either case, there are only two different path contributions to $\hat{T}_a$, where the complex-valued amplitudes t_a^x and t_a^y depend on the intracode tunnel couplings $t_{ll'}$ along the respective paths. They also contain an overall prefactor due to the dot-Majorana tunnel couplings, cf. Eq. (11).

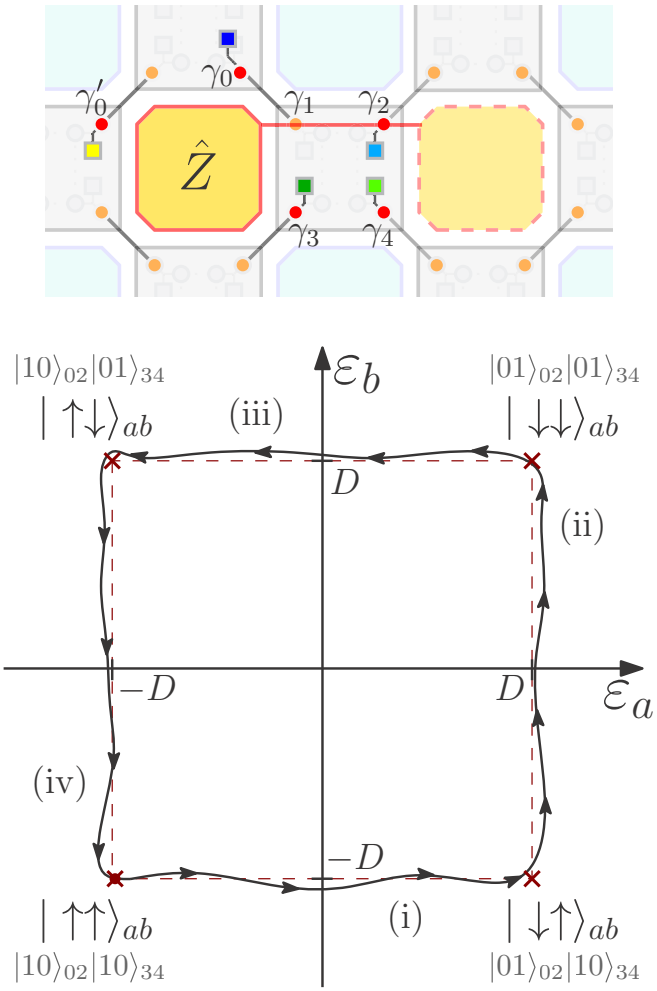

FIG. 6. Upper panel: Phase gate implementation for a Z-type double-cut qubit $(\hat{Z},\hat{X})$, initialized in the eigenstate $|+\rangle$ of the internal string operator $\hat{X} = i\gamma_1\gamma_2$. Two pairs of single-level quantum dots (dark/light blue and dark/light green squares connected to $\gamma_{0/2}$ and $\gamma_{3/4}$, respectively) are activated to pump single electrons through the code. After running a four-step pumping protocol the final qubit state is $|A_\theta\rangle = \hat{P}(\theta)|+\rangle$, where the phase gate operator $\hat{P}(\theta)$ has tunable angle θ, see Eq. (41). By using the alternative dot configuration $0 \to 0'$ (yellow square), parametrically different angles θ can be generated. Lower panel: Schematic illustration of the four-step protocol (32) obtained by sweeping the dot energy levels $\varepsilon_{a/b}$, see Eq. (29), via gate voltages. Intermediate states of the auxiliary (a,b) spin variables are also specified in the physical dot occupation number representation. Straight dashed lines show idealized protocols, where $\varepsilon_a(t)$ during step (iii) is a time-reversed copy of step (i) and similarly for ε_b during steps (ii) and (iv). The solid curve is for a realistic (imperfect) protocol, see the main text.

The first path $\sim t_a^x$ proceeds along the direct $\gamma_0 \to \gamma_1$ link in Fig. 6. Since it includes in- and out-tunneling events via γ_0, the Majorana operator γ_0 appears twice and thus squares out. Hence this contribution to $\hat{T}_a$ involves the internal string operator $\hat{X} = i\gamma_1\gamma_2$, see Eq. (31). The second path involves an additional loop around the stabilizer $\hat{Z}$, which generates the Pauli operator $\hat{Y} = -i\hat{Z}\hat{X}$ and thereby explains the term $\sim t_a^y \hat{Y}$ in Eq. (31). Because of the destructive interference mechanism discussed in Sec. II C, we obtain $t_a^x = 0$ by choosing an integer

backgate parameter n_g (detuning $\Delta n_g \to 0$) for the MCB hosting γ_0. Since t_a^y involves more tunneling events than t_a^x, we can then tune the relative strength of both paths over a wide range, $|t_a^x/t_a^y| \approx \Delta n_g E_C^2/\bar{t}^2$, where $\bar{t}$ denotes a typical value of $|t_{ll'}|$.

Similarly, processes employing the dot pair $b = (3,4)$ can be described in the spin language. Defining spin-1/2 operators $\vec{S}_b$ as in Eq. (30) but with $d_0 \to d_3$ and $d_2 \to d_4$, the effective spin Hamiltonian H_b is as in Eq. (31) with $a \to b$. However, the respective coupling ratio $|t_b^y/t_b^x|$ is now much smaller, since the longer path encircling the $\hat{Z}$ plaquette is both subject to destructive interference and suppressed by orders in $|t_{ll'}|/E_C$, see Fig. 6.

Using a four-step shuffling sequence alternating between dot pairs a and b, single electrons are then transferred back and forth between the two dots in a given pair. This forced transfer process employs interfering tunneling paths running through the code itself and will allow us to manipulate the logical qubit state in a controllable manner. In fact, gate voltage sweeps of $\varepsilon_{a/b}$ are equivalent to independent magnetic field changes, where the field is always oriented along the respective z axis and may induce spin flips $|\uparrow\rangle_{a/b} \to |\downarrow\rangle_{a/b}$ or vice versa. The two spins $\vec{S}_{a,b}$ in turn interact with the code qubit $(\hat{Z},\hat{X})$, see Eq. (31), resulting in a gate-voltage steered motion of the qubit state on the corresponding Bloch sphere. Our protocol starts out from the initial spin configuration $|\uparrow\uparrow\rangle_{ab}$, corresponding to dots 0 and 3 (2 and 4) in an occupied (empty) state. It then consists of four steps, see Fig. 6,

$$|\uparrow\uparrow\rangle_{ab} \xrightarrow{\text{(i)}} |\downarrow\uparrow\rangle_{ab} \xrightarrow{\text{(ii)}} |\downarrow\downarrow\rangle_{ab} \xrightarrow{\text{(iii)}} |\uparrow\downarrow\rangle_{ab} \xrightarrow{\text{(iv)}} |\uparrow\uparrow\rangle_{ab}. \tag{32}$$

After the cycle has been completed, the initial spin configuration is reached again. In each step, either $\varepsilon_a(t)$ [during steps (i) and (iii)] or $\varepsilon_b(t)$ [during (ii) and (iv)] is varied, whereas the respective other parameter is held constant at large absolute value $|\varepsilon_{b/a}| = D \gg |\hat{T}_{b/a}|$, i.e., $H_{b/a}$ does not influence that part of the protocol.

The full system then includes the code qubit $(\hat{Z},\hat{X})$ and the (a,b) spins, i.e., the two dot pairs. We start from the initial product state

$$|\Psi_0\rangle = (\alpha|0\rangle + \beta|1\rangle) \otimes |\uparrow\uparrow\rangle_{ab} = |\psi\rangle \otimes |\uparrow\uparrow\rangle_{ab}, \tag{33}$$

with arbitrary code qubit state $|\psi\rangle$. In order to prepare the ancilla state $|A_\theta\rangle$, one puts $\alpha = \beta = 1/\sqrt{2}$ such that $|\psi\rangle = |+\rangle$, cf. Eq. (28). For a study of the subsequent time evolution under the time-dependent steering protocol in Eq. (32), it is convenient to introduce the effective parity operators

$$\hat{\mathcal{P}}_a = 2S_a^z\hat{Z}, \quad \hat{\mathcal{P}}_b = 2S_b^z\hat{Z}, \quad \hat{\mathcal{P}}_{\text{tot}} = 4S_a^zS_b^z\hat{Z}, \tag{34}$$

which have eigenvalues $\mathcal{P}_{a/b/\text{tot}} = \pm 1$. We observe that during steps (i) and (iii) of the above protocol, $\hat{\mathcal{P}}_a$ is conserved, $[\hat{\mathcal{P}}_a, H] = [\hat{\mathcal{P}}_a, H_a] = 0$, since H_b here reduces to an irrelevant constant as explained above. Similarly, $\hat{\mathcal{P}}_b$ is conserved during steps (ii) and (iv). In addition, the operator $\hat{\mathcal{P}}_{\text{tot}}$ in Eq. (34) is conserved during the entire protocol, and we can separately consider the parity sectors $\mathcal{P}_{\text{tot}} = \pm 1$.

Let us first discuss the $\mathcal{P}_{\text{tot}} = +1$ sector, where one effectively starts from the initial state $|0\rangle \otimes |\uparrow\uparrow\rangle_{ab}$ with amplitude α, see Eq. (33). (For $\mathcal{P}_{\text{tot}} = -1$, see below.) Under the protocol (32), the effective parities $\mathcal{P}_{a,b}$ develop as

$$\begin{aligned} \mathcal{P}_a &= +1 \xrightarrow{\text{(i)}} +1 \xrightarrow{\text{(ii)}} -1 \xrightarrow{\text{(iii)}} -1 \xrightarrow{\text{(iv)}} +1, \\ \mathcal{P}_b &= +1 \xrightarrow{\text{(i)}} -1 \xrightarrow{\text{(ii)}} -1 \xrightarrow{\text{(iii)}} +1 \xrightarrow{\text{(iv)}} +1. \end{aligned} \tag{35}$$

In each step of the protocol, by exploiting conservation of $\mathcal{P}_{\text{tot}}$ and one of the $\mathcal{P}_{a/b}$ parities, only two basis states are dynamically relevant. For instance, during step (i) where $\mathcal{P}_a = +1$ is conserved, those two states are $|0\rangle\otimes|\uparrow\uparrow\rangle_{ab}$ and $|1\rangle \otimes |\downarrow\uparrow\rangle_{ab}$. On the other hand, during step (iii) with conserved parity value $\mathcal{P}_a = -1$, they are given by $|0\rangle \otimes |\downarrow\downarrow\rangle_{ab}$ and $|1\rangle \otimes |\uparrow\downarrow\rangle_{ab}$, see Fig. 6. The physics during step (i) and (iii) is then described by the respective simple 2×2 Hamiltonian

$$H_a^{(\mathcal{P}_a=\pm 1)} = \begin{bmatrix} \varepsilon_a & i\left(t_a^x \mp t_a^y\right) \\ -i\left(t_a^x \mp t_a^y\right)^* & -\varepsilon_a \end{bmatrix}. \tag{36}$$

The corresponding Hamiltonian for steps (ii) and (iv) follows by letting $a \to b$ in Eq. (36). Similarly, by taking into account the constraints (35) and the above discussion, the state after each of the four steps in Eq. (32) will be given by

$$\begin{aligned} |0\rangle \otimes |\uparrow\uparrow\rangle_{ab} \xrightarrow{\text{(i)}} |1\rangle \otimes |\downarrow\uparrow\rangle_{ab} \xrightarrow{\text{(ii)}} |0\rangle \otimes |\downarrow\downarrow\rangle_{ab} \xrightarrow{\text{(iii)}} \\ \xrightarrow{\text{(iii)}} |1\rangle \otimes |\uparrow\downarrow\rangle_{ab} \xrightarrow{\text{(iv)}} |0\rangle \otimes |\uparrow\uparrow\rangle_{ab}, \end{aligned} \tag{37}$$

up to a crucial phase factor discussed next.

We now analyze the steered qubit motion on its Bloch sphere in more detail. During step (i), spin a is flipped, $|\uparrow\rangle_a \to |\downarrow\rangle_a$, and the qubit state is dragged from the north to the south pole, $|0\rangle \to |1\rangle$, at azimuthal angle

$$\delta^{(\text{i})}_{\mathcal{P}_a=+} = \arg\left[-i\left(t_a^x - t_a^y\right)^*\right]. \tag{38}$$

Since the entire qubit motion proceeds under this angle, the latter can be read off from $H_a^{(\mathcal{P}_a=+1)}$ by letting $\varepsilon_a \to 0$, see Eq. (36). In the next step (ii), which is governed by $H_b^{(\mathcal{P}_b=-1)}$, spin b is also flipped by a respective gate sweep applied to dot pair (3,4). Thereby the code qubit is forced to move back to the north pole but under the different azimuthal angle

$$\delta^{(\text{ii})}_{\mathcal{P}_b=-1} = \arg\left[-i\left(t_b^x + t_b^y\right)^*\right]. \tag{39}$$

This difference to Eq. (38) arises because spin b employs the transfer operator $\hat{T}_b$ instead of $\hat{T}_a$. We then proceed with step (iii), where spin a returns to the state $|\uparrow\rangle_a$ and thereby drives the qubit once more from north to south pole. This happens at the azimuthal angle $\delta_-^{(\text{iii})} = \arg[i(t_a^x + t_a^y)]$. In the final step (iv), spin b is also flipped back to $|\uparrow\rangle_b$. With $\delta_+^{(\text{iv})} = \arg[i(t_b^x - t_b^y)]$, we thus have returned to the initial state up to a phase factor.

The logical qubit state has then been steered twice from north to south pole (and back) on the Bloch sphere. Dynamical phases always cancel out under this protocol (see below), and the phase acquired by the qubit state has a purely geometric origin. This non-Abelian Berry phase can be obtained from the solid angle $\Omega_{\mathcal{P}_{\text{tot}}=+1}$ encircled during a full cycle on the Bloch sphere as $\theta = \Omega_+/2$ [70]. Since we move directly between both poles (with different azimuthal angles), one easily obtains

$$\frac{\Omega_+}{4\pi} = \frac{1}{2\pi}[\delta_+^{(\text{i})} - \delta_-^{(\text{ii})} + \delta_-^{(\text{iii})} - \delta_+^{(\text{iv})}]. \tag{40}$$

The Berry phase can thus be decomposed into two parts depending only on $t_a^{x,y}$ or $t_b^{x,y}$ parameters. With $\theta_a = \delta_+^{(\mathrm{i})} + \delta_-^{(\mathrm{iii})}$ and $\theta_b = -(\delta_-^{(\mathrm{ii})} + \delta_+^{(\mathrm{iv})})$, we find

$$\theta = \theta_a + \theta_b,$$
$$\theta_{a/b} = \tan^{-1}\left(\frac{2\left|t_{a/b}^x t_{a/b}^y\right|}{\left|t_{a/b}^x\right|^2 - \left|t_{a/b}^y\right|^2}\sin\varphi_{a/b}\right), \tag{41}$$

where $\varphi_{a/b}$ is the relative phase difference between $t_{a/b}^x$ and $t_{a/b}^y$. As discussed above, the regime with $|t_b^y/t_b^x| \ll 1$ is naturally expected for the setup in Fig. 6, resulting in $\theta_b \to 0$ and hence $\theta \simeq \theta_a$.

To complete the discussion, we now address the other parity sector $\mathcal{P}_{\mathrm{tot}} = -1$, where one starts out from the initial state $|1\rangle \otimes |\uparrow\uparrow\rangle_{ab}$ with amplitude β, cf. Eq. (33). The corresponding time evolution can be recovered from the above expressions for $\mathcal{P}_{\mathrm{tot}} = +1$ by the replacement $\mathcal{P}_{a/b} \to -\mathcal{P}_{a/b}$, implying $\delta_+^{(\mathrm{i,ii,iii,iv})} \leftrightarrow \delta_-^{(\mathrm{i,ii,iii,iv})}$ in Eq. (40). Further taking into account that the tunneling processes (i) and (iii) [and (ii) and (iv)] are related by Hermitian conjugation, i.e.,

$$\delta_\pm^{(\mathrm{iii})} = -\delta_\pm^{(\mathrm{i})}, \quad \delta_\pm^{(\mathrm{iv})} = -\delta_\pm^{(\mathrm{ii})}, \tag{42}$$

the solid angle for $\mathcal{P}_{\mathrm{tot}} = -1$ follows as $\Omega_- = -\Omega_+$, and hence the Berry phase $-\theta$ will be picked up. In effect, with $\alpha = \beta = 1/\sqrt{2}$ in Eq. (33), i.e., by preparing the qubit in the $|+\rangle$ state, the final state after running the four-step protocol is precisely given by the ancilla state $|A_\theta\rangle$ in Eq. (28). Remarkably, we can thereby realize a static and parametrically tunable phase angle θ, see Eq. (41). With $\theta \simeq \theta_a$, a main handle to adjust this angle is given by the backgate detuning parameter Δn_g on the MCB hosting γ_0, see Fig. 6. Assuming small detuning, $|\Delta n_g| \ll 1$, we find $\theta \sim |t_a^x/t_a^y| \sim \Delta n_g E_C^2/\bar{t}^2$ up to the prefactors in Eq. (41).

By alternative choices of dots for the pump protocol, one may change the parametric dependencies of the phase gate angle θ. Using the quantum dot $0 \to 0'$ (yellow square) in Fig. 6, the ratio of tunneling amplitudes $|t_a^x/t_a^y|$ becomes independent of the scale $\bar{t}/E_c$. Still, now adjusting the backgate parameter n_g' of the box hosting γ_0' in Fig. 6, one may tune and/or quench the tunneling amplitude t_a^x. To leading order, the protocol then yields the phase angle $\theta \sim \Delta n_g'$ while $\bar{t}/E_c$ can be changed independently.

Last, we address the effect of errors, see also Sec. IV F below. First, energy splittings between the $Z = \pm$ qubit states can result from the static stabilizer Hamiltonian (5) or from the Majorana-dot tunnel couplings entering the pumping Hamiltonian, cf. Eq. (36). However, noting that our four-step protocol involves intermediate parity flips in both subsectors, $\mathcal{P}_{a/b} \to -\mathcal{P}_{a/b}$, we observe that as long as the control parameters $\varepsilon_{a/b}(t)$ run back and forth in a time-reversed manner during the respective steps (i) and (iii) and then (ii) and (iv), dynamical phases cancel out automatically. Even under imperfect gate control, see the lower panel of Fig. 6, such contributions are expected to echo out. In particular, by $n > 1$ repetitions of a protocol with small phase angle θ/n, the Berry phase θ comes with a more efficient cancellation of dynamical phases. Second, assuming time-reversed gate sweeps, the four-step pumping sequence (32) affords a topological protection in the control parameter space $(\varepsilon_a, \varepsilon_b)$, i.e., the pumped phase will be independent of the precise time dependence of $\varepsilon_{a/b}(t)$ as long as the intermediate steps of the protocol in Eq. (32) are reached. Third, we note that small deviations from adiabaticity are permitted if diabatic errors are eliminated by intermediate charge measurements on the dots [68]. We emphasize that the static code parameters yielding θ in Eq. (41) can be adjusted and fine-tuned. Since the protocol forms a closed loop in control parameter space, in principle, it can be run indefinitely. For instance, after preparing the desired ancilla state $|A_\theta\rangle$, this state can be postprocessed or verified by state tomography. One can then readjust the code parameters in order to optimize the protocol. Finally, charge dephasing may be a challenge, in particular if the anticrossing energy $|\hat{T}_{a/b}|$ is very small. Extensions of the protocol (cf. Refs. [68,71]) should be possible and can be used to tackle some of the challenges outlined here. We leave a detailed investigation to future work.

To conclude, the presented phase gate protocol follows from a gate-steered rotation in the hybrid low-energy subspaces of the quantum dots and the code qubit. Such control and rotations are possible since single-electron tunneling events generate logical string operators acting on the code space, see Sec. II C. As electrons traverse the code, these strings drag along Z- and X-type excitations, which can be created and braided in nontrivial interleaved pumping sequences. In the manipulations applied to our code architecture, the coupling to different Pauli operators or strings naturally arises from superpositions of tunneling paths through the code.

F. Errors and challenges

Having discussed a framework of elemental quantum logical operations sufficient to the implementation of gates, we are now in position to address likely sources of errors or other physical mechanisms detrimental to the functioning of the system. Generally speaking, we expect the topological protection of the elementary Majorana particles (on which our approach is based) to manifest itself in long coherence and qubit lifetimes. This may turn out to be an important mechanism keeping the need for active error correction at tolerably low levels. Second, a general advantage of the stabilizer code approach is that Clifford gates do not require active error correction [58]. Measurement errors then merely need to be kept track of, which can be done by classical software [10]. We thus are confident that the present Majorana-based code can be implemented with a reasonably low operational overhead. Likely error sources and/or challenges include the following.

1. Dynamical phase errors

These errors are caused by the effectively random (but static) coupling constants generated by tunneling processes encircling single or multiple stabilizers. As a consequence, the time evolution even of stationary states leads to dynamical phases. The ensuing errors are correctable if, in each cycle, they affect less than half of the stabilizers defining an encoded logical qubit [10,11]. Generally, it will thus be advantageous to reduce or quench off the tunnel couplings contributing to a logical qubit. Increasing the physical to logical qubit ratio then exponentially suppresses the remaining detrimental tunneling

terms and therefore provides exponential protection against dephasing errors.

2. MCB errors

A second class of dynamical errors has its origin in the less-than-perfect design of the MCBs. The functioning of our approach rests on the approximate degeneracy of the two quantum states realized by a MCB in the strong charging limit. That qubit degeneracy gets lifted when the Majoranas constituting it hybridize with each other, e.g., due to the finite length of the MCB semiconductor quantum wires. The actual splitting for realistic geometries is not yet known and additional experiments on simple Majorana-based qubits will be needed to estimate these error rates. In terms of MCB Pauli operators (2), such residual overlaps act as effective magnetic fields. In general, these Pauli errors are correctable.

A qualitatively different class of errors originates in quasiparticle poisoning. For example, quasiparticles may jump on and off neighboring MCBs. Such processes are efficiently suppressed by the charging energy, which in practice results in charge stability over very long times (hours). Nonetheless, quasiparticle poisoning can have detrimental consequences to the operation of the surface code when Cooper pairs on a given MCB are likely to break up—a process which has been experimentally verified to occur at time scales beyond 10 ms for single nanowires [25]. If the electrons recombine with two different Majorana states, then this will create a Pauli error, which is straightforward to detect via an observable change of the stabilizer states connecting to the MCB. Such Pauli errors can again be corrected. On the other hand, if only one quasiparticle recombines with a Majorana state, the error is hard to correct since the system leaves the computational subspace. Such an event will manifest itself in a flip of the fermion parity operator $\hat{\mathcal{P}}_l$ on a single MCB, in addition to flips of the adjacent $\hat{Z}$ and $\hat{X}$ stabilizers. This error is not correctable anymore, since we do not read out the operator $\hat{\mathcal{P}}_l$ needed to unambiguously detect it in the present scheme.

Once such an error has occurred, we are left with an out-of-subspace Majorana system plus an isolated quasiparticle. The latter may remain idle on the MCB for some time. Eventually, the original state of the system gets restored (vanishing of the error) or recombination with another Majorana state takes place (return to the computational subspace plus a Pauli error). If the out-of-subspace time exceeds typical operation times and/or quasiparticle poisoning errors occur on logical qubits, then the functioning of the code gets compromised. Fortunately, errors of this type betray themselves via correlated flips of neighboring stabilizers $\hat{Z}$ and $\hat{X}$. If they turn out to be important, then measurements of the box parity operators $\hat{P}_l$ should be implemented. However, this will require a more modified approach than presented here.

3. Conductance interferometry and readout scheme

Our conductance readout schemes require reference arms for path interference. Quantum coherence will only be preserved if the length of these arms is shorter than the phase coherence length in the relevant material. Since the distance between (zero-energy) Majorana states on a given MCB should be larger than the coherence length in the topological superconductor [13,14], this sets a minimum length for the reference arms as well. The magnitude of a realistic topological gap is not known, but one expects a decay length of Majorana states in the μm regime [26]. However, even if the coherence length of the reference arm is of order μm, the conductance measurement has to be done at low voltages to avoid decoherence of interference signals. All factors considered, it might be favorable to use a topological wire to extend the coherence of the reference arm, similarly to the interferometer suggested by Fu [46]. (We note that such long links are needed only along the wire direction in Fig. 1.) Again one will have to rely on experimental progress to determine what the best solution is, and therefore we leave this as an open challenge.

Another important issue is to perform stabilizer measurements on a sufficiently fast time scale. However, the conductance in the readout scheme will be small because the MCBs are operated in the cotunneling regime, and hence the necessary integration time might be long. Fortunately, there are also different measurable quantities that rely on the same topological interferometry as discussed here. One possibility is to read out tunneling times by charge measurements, which means that one could change the design by replacing the normal leads with dots and charge sensors [57]. This is a known technology with readout times below microseconds [72] and offers the advantage that only one dot needs to be coupled to each Majorana state (instead of a lead and a dot). Also in this case, actual experimental realizations will determine the best strategy. An interesting question, where the answer depends on the actual readout strategy, is how fast a projective measurement can be. It will also be important to understand better, on a theoretical level, the time scales for projective measurements when the measured quantities are tunneling rates rather than the transferred charge.

4. 2D vs 3D architecture

When discussing hardware solutions, errors, and their countering, one should have in mind that the 3D integration envisioned in Ref. [12], cf. also Fig. 1, with controllable tunnel junctions connecting the code to another layer containing gate electrodes and probe leads, may be difficult to realize. This is not a fundamental obstacle but something that still needs to be developed along with the topological wire layouts. The first demonstration experiments should therefore be designed in a purely 2D setup [57], where one can also address charge vs conductance readout and the role of quasiparticle poisoning.

V. LOGICAL GATES FOR UNIVERSAL QUANTUM COMPUTATION

We now turn to logical gates in the present code architecture, which can be implemented by known quantum circuits [10,19,58,73] once the basal quantum operations in Sec. IV have been realized. We consider the set $\{\hat{C},\hat{H},\hat{S},\hat{T}\}$ of elementary gates, containing the CNOT $\hat{C}$, the Hadamard $\hat{H}$, and the phase gates $\hat{S}$ and $\hat{T}$. This set is sufficient for universal quantum computation [58]. Since $\hat{T}^2=\hat{S}$, the $\hat{S}$ gate is formally not necessary for a minimal set, but access to a simple and efficient realization is highly desired in practice.

A. Controlled-NOT gate

We first recall that in the Schrödinger picture, the CNOT acts on a two-qubit state as $|\psi_A\rangle \otimes |\psi_B\rangle \to \hat{C}(|\psi_A\rangle \otimes |\psi_B\rangle)$, where the unitary operator

$$\hat{C} = \frac{(\hat{I}+\hat{Z})_A}{2} \otimes \hat{I}_B + \frac{(\hat{I}-\hat{Z})_A}{2} \otimes \hat{X}_B \tag{43}$$

flips the target qubit B iff the control qubit A is in a down-state [58]. The Schrödinger description of $\hat{C}$ in Eq. (43) is equivalent to a Heisenberg transformation, $\hat{\mathcal{O}}_A \otimes \hat{\mathcal{O}}_B \to \hat{C}^{-1}(\hat{\mathcal{O}}_A \otimes \hat{\mathcal{O}}_B)\hat{C}$. This transformation is recovered by the braiding-induced manipulation of operators in Eq. (23), see Sec. IV C. Since all other transformations of the two-qubit operator algebra can be constructed from Eq. (23), those four rules are sufficient to fully characterize the CNOT gate [58]. As shown in Sec. IV C, cf. also Fig. 4, the rules in Eq. (23) can be directly implemented by braiding a pair of different-type logical qubits. We note that the CNOT operation for same-type qubits can also be obtained by a variant of our protocol. However, since braiding is limited to different-type qubits, one then needs additional ancilla qubits serving as target of an intermediate CNOT, cf. Refs. [10,19]. Last, as both qubit move and braid operations allow for straightforward iteration on qubits with larger stabilizer and/or string distances ($d > 1$), the corresponding extension of the CNOT follows directly.

B. Hadamard gate

The Hadamard gate applies the operator $\hat{H} = (\hat{X}+\hat{Z})/\sqrt{2}$ on a single logical qubit state, $|\psi\rangle \to \hat{H}|\psi\rangle$, mapping Z eigenstates $|0\,/1\rangle$ to X eigenstates $|+/-\rangle$ (Schrödinger) or, equivalently, exchanging $\hat{X}/\hat{Z} \to \hat{Z}/\hat{X}$ (Heisenberg) [58]. An important advantage of the Majorana surface code comes from the fact that the $\hat{H}$ gate can be realized by moving logical information between adjacent qubits of different (X/Z) type [19]. This process effectively exchanges $\hat{X}$ and $\hat{Z}$ operators. Fortunately, such moves can be performed in a rather simple manner in our code architecture, see Sec. IV B. The key ingredient is an interferometric conductance measurement of a string operator, as illustrated in Fig. 3 for the case of minimal string extension (with code distance $d = 1$). An alternative scheme employs stabilizer product operators, see also Sec. IV B.

In order to improve error resilience, a $d > 1$ generalization of either approach to qubits with longer connecting strings and/or larger holes is possible. In the latter case, sequential application of the above manipulations to all constituent elementary qubits implements the Hadamard gate. Similarly, for longer strings, $\approx d$ sequential nonstabilizer measurements are needed. Fault tolerance is then retained because all measured operators commute with local pairs of $\hat{Z}$- and $\hat{X}$-type stabilizer (or string) operators, thus allowing for error checks.

C. *S* gate

We now turn to the implementation of the $\hat{S}$ gate, which acts on a single logical qubit state $|\psi\rangle$ by creating a $\pi/2$ phase shift between the up- and down-components. Using the phase gate operator $\hat{P}(\theta) = e^{i\theta\hat{Z}}$ in Eq. (27), this is achieved by the operator

$$\hat{S} = e^{i\pi/4}\hat{P}(-\pi/4) = \mathrm{diag}(1,i). \tag{44}$$

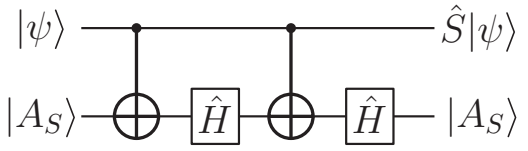

FIG. 7. Quantum circuit for $\hat{S}$-gate implementation [10]. We start from $|\Psi\rangle_{\text{initial}} = |\psi\rangle \otimes |A_S\rangle$, with an arbitrary state $|\psi\rangle$ stored on the logical qubit and the Y eigenstate $|A_S\rangle$, see Eq. (45), on the ancilla qubit. One then applies a CNOT (with the ancilla as target), followed by a Hadamard on the ancilla. Repeating this sequence once more, one arrives at $|\Psi\rangle_{\text{final}} = (\hat{S}|\psi\rangle) \otimes |A_S\rangle$.

To realize the $\hat{S}$ gate, we consider the two-qubit protocol in Fig. 7 [10,58], which employs an ancilla qubit in addition to the logical qubit. Here the ancilla is prepared in the Pauli-Y eigenstate

$$|A_S\rangle = \hat{S}|+\rangle = (|0\rangle + i|1\rangle)/\sqrt{2}, \tag{45}$$

or, equivalently, $|\bar{A}_S\rangle = \hat{S}^\dagger|+\rangle$. Note that $\hat{Y}|A_S\rangle = |A_S\rangle$ and $\hat{Y}|\bar{A}_S\rangle = -|\bar{A}_S\rangle$, where $|A_S\rangle$ is equivalent to $|A_{\theta=-\pi/4}\rangle$ in Eq. (28). By applying a sequence of CNOT and Hadamard gates, the circuit in Fig. 7 arrives (in the absence of errors) at the product state $|\Psi\rangle_{\text{final}} = (\hat{S}|\psi\rangle) \otimes |A_S\rangle$, containing the desired state $\hat{S}|\psi\rangle$ on the logical qubit. At the same time, one recovers the original ancilla state.

The $\hat{S}$-gate implementation then boils down to a reliable generation of $|A_S\rangle$ ancilla states. In principle, these could be obtained by direct $\hat{Y}$ measurements on the qubits of the code. However, since many ancilla states have to be generated in practice, an attractive alternative is offered by the state injection approach in Sec. IV D. Here one first prepares MCB Pauli-$\hat{y}$ states on a separate auxiliary box. In a second step, this MCB qubit state is transferred (injected) to a selected ancilla qubit in the code. Given that this preparation scheme relies on projective measurements, the obtained states are expected to naturally have high fidelity with $|A_S\rangle$ in Eq. (45) [74], possibly obviating the need for magic state distillation [5]. This route can offer a significant reduction of the large ancilla preparation overhead needed in other surface code architectures (see, e.g., Ref. [10] and references therein) and could thereby pave the way towards an efficient experimental realization of Clifford operations.

D. *T* gate

With the set $\{\hat{C},\hat{H},\hat{S}\}$ discussed up to now, we can only perform Clifford operations [58]. The Gottesman-Knill theorem [75] states that a Clifford-only quantum computer offers no quantum speedup since Clifford-based computations can be carried out efficiently on a classical computer [11]. Although such a system can still be highly useful as platform for many QIP tasks, universal quantum computation requires an additional non-Clifford gate, for example the $\hat{T}$ gate [58].

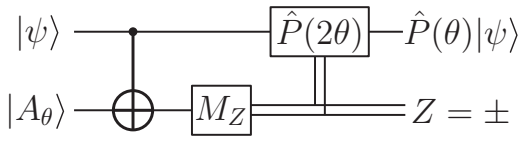

FIG. 8. Quantum circuit for implementing a phase gate $\hat{P}(\theta)$, see Eq. (27), with arbitrary angle θ [73]. The $\hat{T}$ gate follows for $\theta = -\pi/8$, see Eq. (46). Starting from the two-qubit state $|\Psi\rangle_{\text{initial}} = |\psi\rangle \otimes |A_\theta\rangle$, with arbitrary state $|\psi\rangle$ on the logical qubit and the ancilla state $|A_\theta\rangle$ in Eq. (28), a CNOT is followed by a Pauli-Z measurement (M_Z) on the ancilla (outcome $Z = \pm 1$). Double lines indicate classical information processing, where $\hat{P}(2\theta)$ is applied to the logical qubit iff $Z = -1$. The final logical qubit state is $\hat{P}(\theta)|\psi\rangle$.

This gate is equivalent to the $\theta = -\pi/8$ phase gate,

$$\hat{T} = e^{i\pi/8}\hat{P}(-\pi/8) = \text{diag}(1, e^{i\pi/4}), \tag{46}$$

and is also used to achieve universality in other Majorana-based quantum computation approaches, see, e.g., Refs. [38,71]. Possibly with minor modifications, our proposal, see Sec. IV E and below, can be useful to (or make use of) those schemes as well.

Our phase gate implementation uses the quantum circuit in Fig. 8, which entangles a logical qubit containing an arbitrary state $|\psi\rangle$ with an ancilla qubit state $|A_\theta\rangle$. The latter follows by applying $\hat{P}(\theta)$ to the $|+\rangle$ eigenstate of the ancilla, see Eq. (28). After a CNOT, one measures the ancilla Pauli-Z component (outcome $Z = \pm 1$). For $Z = +1$, one directly obtains the desired state $\hat{P}(\theta)|\psi\rangle$ on the logical qubit. However, for $Z = -1$, one obtains $\hat{P}(-\theta)|\psi\rangle$ and then has to apply the operator $\hat{P}(2\theta)$ to correct the result. Since, for $\theta = -\pi/8$, the operator $\hat{P}(2\theta)$ represents the relatively simple Clifford operation $\hat{S}$ in Eq. (44), when using the circuit in Fig. 8, the $\hat{T}$ gate will be much easier to realize than arbitrary-θ phase gates. The above protocol also can be used to implement the $\hat{S}$ gate ($\theta = -\pi/4$), where $\hat{P}(2\theta)$ is equivalent to the Pauli operator $\hat{Z}$. However, since one here loses the ancilla state, the $\hat{S}$-gate implementation in Sec. V C is more efficient if ancilla preparation constitutes the bottleneck.

In order to implement the $\hat{T}$ gate in our code architecture, one may first generate the ancilla states $|A_{\theta=-\pi/8}\rangle$ by the multistep electron pumping protocol in Sec. IV E. These states are then processed by the circuit in Fig. 8, which yields the desired logical qubit gate, $\hat{T}|\psi\rangle$. For elementary QIP tasks and first experimental checks, we expect that our pumping protocol can directly yield ancilla states of sufficiently high fidelity. In such basic cases, phase gate operations may directly be applied to logical qubit states without the need for additional magic state distillation steps [5], thus resulting in a significantly reduced overhead in both hardware and operation. The above route towards tunable phase gates also works for setups composed of a few elementary MCB qubits [57].

VI. CONCLUSIONS

We have discussed a Majorana surface code platform based on topological semiconductor qubits, where the nodes of the network are Majorana-Cooper boxes hosting four Majorana bound states. The fermion parity of each MCB is fixed by the charging energy, leading to a two-level (spin-1/2) system protected by the nonlocal properties of Majorana states. These nonlocal properties give a natural anisotropic coupling [18] between neighboring MCBs, which is ideal for a surface code implementation where stabilizers, consisting of products of $\hat{x}$ or $\hat{z}$ Pauli operators surrounding a plaquette, are being measured. Building on this platform, we here took the crucial next step to introduce concrete and arguably realistic ways of operating this surface code architecture. It is worth noting that the Majorana surface code avoids the use of extra measurement qubits as in bosonic codes [10,43–45], where our readout protocols are based on interfering electron paths.

The surface code architecture presented here offers a fault-tolerant set of gates, including CNOT and Hadamard. To complete the group of Clifford gates, we have shown how the $\hat{S}$ gate can be implemented via state injection of an ancilla state into the code, which for advanced QIP tasks may be augmented by a magic state distillation protocol. In order to make the surface code computation universal, one needs a single non-Clifford gate, for example, a phase gate with arbitrary phase angle. We here take advantage of the unique characteristics of the Majorana surface code hardware to propose qualitatively new implementations of gate operations in terms of a multistep single-electron pumping protocol. This protocol has the interesting property that it always gives a phase gate, where the phase angle of the gate is protected in the sense that it depends on fixed and tunable tunnel coupling amplitudes but not on the detailed timing of the protocol, cf. Sec. IV E. In this respect, it is similar to other schemes for adiabatic non-Clifford gates [33,38]. We finally note that the adiabatic approximation can be partially circumvented in our protocol if confirmation measurements ensure that the expected final state has been reached. It is worth mentioning that an alternative and completely measurement-based universal approach using Ising genons in Majorana wire networks has recently been proposed in Ref. [76].

In view of currently unknown experimental perspectives, the realization of hybrid platforms comprising different types of Majorana-based architectures [30–39] may offer practical advantages. With the state injection protocol in Sec. IV D, we have proposed a route to couple other systems to the Majorana surface code or to related setups composed of MCB-based qubits. To investigate the feasibility of our surface code proposal, first experimental tests should focus on select building blocks of the full setup. This will allow one to characterize important system parameters, e.g., lifetimes of MCB qubits, readout times, and so on. Among the first steps could be to demonstrate error correction in devices containing a few qubits, similar to what has been done for bosonic codes with superconducting qubits [41–43,45]. Besides considering specific error correction schemes, such tests would also be necessary to investigate the feasibility of using MCBs as fundamental qubits.

To conclude, we hope that our proposal will stimulate further experimental and theoretical work towards quantum computation based on Majorana systems. In particular, we believe that the idea of using parity-fixed Majorana boxes with four Majorana states as elementary qubits opens very promising perspectives in this context.

ACKNOWLEDGMENTS

We thank S. Albrecht, P. Bonderson, M. Freedman, L. Fu, D. Gross, F. Hassler, H. Kampermann, C. Marcus, and A. Rasmussen for inspiring discussions. We acknowledge funding by the Deutsche Forschungsgemeinschaft (Bonn) within CRC network TR 183 (A.A., K.F., R.E.), by the Danish National Research Foundation and Microsoft Research (K.F.), by the Israel Science Foundation Grant No. 1243/13 (E.S.), and by the Marie Curie CIG Grant No. 618188 (E.S.).

[1] D. Gottesman, Stabilizer codes and quantum error correction, Ph.D. thesis, Caltech, 1997.

[2] S. Bravyi and A. Kitaev, Quantum codes on a lattice with boundary, Quant. Comput. Comput. **2**, 43 (2001).

[3] M. H. Freedman and D. A. Meyer, Projective plane and planar quantum codes, Found. Comput. Math. **1**, 325 (2001).

[4] E. Dennis, A. Kitaev, A. Landahl, and J. Preskill, Topological quantum memory, J. Math. Phys. **43**, 4452 (2002).

[5] S. Bravyi and A. Kitaev, Universal quantum computation with ideal Clifford gates and noisy ancillas, Phys. Rev. A **71**, 022316 (2005).

[6] R. Raussendorf and J. Harrington, Fault-Tolerant Quantum Computation with High Threshold in Two Dimensions, Phys. Rev. Lett. **98**, 190504 (2007).

[7] R. Raussendorf, J. Harrington, and K. Goyal, Topological fault-tolerance in cluster state quantum computation, New J. Phys. **9**, 199 (2007).

[8] D. S. Wang, A. G. Fowler, and L. C. L. Hollenberg, Surface code quantum computing with error rates over 1%, Phys. Rev. A **83**, 020302(R) (2011).

[9] A. G. Fowler, A. C. Whiteside, and L. C. L. Hollenberg, Towards Practical Classical Processing for the Surface Code, Phys. Rev. Lett. **108**, 180501 (2012).

[10] A. G. Fowler, M. Mariantoni, J. M. Martinis, and A. N. Cleland, Surface codes: Towards practical large-scale quantum computation, Phys. Rev. A **86**, 032324 (2012).

[11] B. A. Terhal, Quantum error correction for quantum memories, Rev. Mod. Phys. **87**, 307 (2015).

[12] L. A. Landau, S. Plugge, E. Sela, A. Altland, S. M. Albrecht, and R. Egger, Towards Realistic Implementations of a Majorana Surface Code, Phys. Rev. Lett. **116**, 050501 (2016).

[13] J. Alicea, New directions in the pursuit of Majorana fermions in solid state systems, Rep. Prog. Phys. **75**, 076501 (2012).

[14] M. Leijnse and K. Flensberg, Introduction to topological superconductivity and Majorana fermions, Semicond. Sci. Technol. **27**, 124003 (2012).

[15] C. W. J. Beenakker, Search for Majorana fermions in superconductors, Annu. Rev. Con. Mat. Phys. **4**, 113 (2013).

[16] S. Das Sarma, M. Freedman, and C. Nayak, Majorana zero modes and topological quantum computation, Quant. Inform. **1**, 15001 (2015).

[17] S. Bravyi, B. M. Terhal, and B. Leemhuis, Majorana fermion codes, New J. Phys. **12**, 083039 (2010).

[18] B. M. Terhal, F. Hassler, and D. P. DiVincenzo, From Majorana Fermions to Topological Order, Phys. Rev. Lett. **108**, 260504 (2012).

[19] S. Vijay, T. H. Hsieh, and L. Fu, Majorana fermion surface code for universal quantum computation, Phys. Rev. X **5**, 041038 (2015).

[20] S. Vijay and L. Fu, Physical implementation of a Majorana surface code for fault-tolerant quantum computation, Phys. Scr. **T168**, 014002 (2016).

[21] Y. Li, Noise Threshold and Resource Cost of Fault-Tolerant Quantum Computing with Majorana Fermions in Hybrid Systems, Phys. Rev. Lett. **117**, 120403 (2016).

[22] V. Mourik, K. Zuo, S. M. Frolov, S. R. Plissard, E. P. A. Bakkers, and L. P. Kouwenhoven, Signatures of Majorana fermions in hybrid superconductor-semiconductor nanowire devices, Science **336**, 1003 (2012).

[23] W. Chang, S. M. Albrecht, T. S. Jespersen, F. Kuemmeth, P. Krogstrup, J. Nygård, and C. M. Marcus, Hard gap in epitaxial semiconductor-superconductor nanowires, Nat. Nanotech. **10**, 232 (2015).

[24] P. Krogstrup, N. L. B. Ziino, W. Chang, S. M. Albrecht, M. H. Madsen, E. Johnson, J. Nygård, C. M. Marcus, and T. S. Jespersen, Epitaxy of semiconductor-auperconductor nanowires, Nat. Mat. **14**, 400 (2015).

[25] A. P. Higginbotham, S. M. Albrecht, G. Kirsanskas, W. Chang, F. Kuemmeth, T. S. Jespersen, J. Nygård, K. Flensberg, and C. M. Marcus, Parity lifetime of bound states in a proximitized semiconductor nanowire, Nat. Phys. **11**, 1017 (2015).

[26] S. M. Albrecht, A. P. Higginbotham, M. Madsen, F. Kuemmeth, T. S. Jespersen, J. Nygård, P. Krogstrup, and C. M. Marcus, Exponential protection of zero modes in Majorana islands, Nature **531**, 206 (2016).

[27] H. Zhang *et al.*, Ballistic Majorana nanowire devices, arXiv:1603.04069.

[28] J. Shabani *et al.*, Two-dimensional epitaxial superconductor-semiconductor heterostructures: A platform for topological superconducting networks, Phys. Rev. B **93**, 155402 (2016).

[29] M. Kjaergaard *et al.*, Quantized conductance doubling and hard gap in a two-dimensional semiconductor-superconductor heterostructure, Nat. Commun. **7**, 12841 (2016).

[30] J. D. Sau, S. Tewari, and S. Das Sarma, Universal quantum computation in a semiconductor quantum wire network, Phys. Rev. A **82**, 052322 (2010).

[31] J. Alicea, Y. Oreg, G. Refael, F. von Oppen, and M. P. A. Fisher, Non-Abelian statistics and topological quantum information processing in 1D wire networks, Nat. Phys. **7**, 412 (2011).

[32] D. J. Clarke, J. D. Sau, and S. Tewari, Majorana fermion exchange in quasi-one-dimensional networks, Phys. Rev. B **84**, 035120 (2011).

[33] K. Flensberg, Non-Abelian Operations on Majorana Fermions, Phys. Rev. Lett. **106**, 090503 (2011).

[34] M. Leijnse and K. Flensberg, Quantum Information Transfer Between Topological and Spin Qubit Systems, Phys. Rev. Lett. **107**, 210502 (2011).

[35] P. Bonderson and R. M. Lutchyn, Topological Quantum Buses: Coherent Quantum Information Transfer Between Topological and Conventional Qubits, Phys. Rev. Lett. **106**, 130505 (2011).
[36] T. Hyart, B. van Heck, I. C. Fulga, M. Burrello, A. R. Akhmerov, and C. W. J. Beenakker, Flux-controlled quantum computation with Majorana fermions, Phys. Rev. B **88**, 035121 (2013).
[37] F. L. Pedrocchi and D. P. DiVicenzo, Majorana Braiding with Thermal Noise, Phys. Rev. Lett. **115**, 120402 (2015).
[38] D. J. Clarke, J. D. Sau, and S. Das Sarma, A Practical Phase Gate for Producing Bell Violations in Majorana Wires, Phys. Rev. X **6**, 021005 (2016).
[39] S. Hoffman, C. Schrade, J. Klinovaja, and D. Loss, Universal quantum computation with hybrid spin-Majorana qubits, Phys. Rev. B **94**, 045316 (2016).
[40] D. Aasen *et al.*, Milestones Toward Majorana-Based Quantum Computing, Phys. Rev. X **6**, 031016 (2016).
[41] R. Barends *et al.*, Superconducting quantum circuits at the surface code threshold for fault tolerance, Nature **508**, 500 (2014).
[42] E. Jeffrey *et al.*, Fast Accurate State Measurement with Superconducting Qubits, Phys. Rev. Lett. **112**, 190504 (2014).
[43] A. D. Córcoles, E. Magesan, S. J. Srinivasan, A. W. Cross, M. Steffen, J. M. Gambetta, and J. M. Chow, Demonstration of a quantum error detection code using a square lattice of four superconducting qubits, Nat. Commun. **6**, 6979 (2015).
[44] C. D. Hill, E. Peretz, S. J. Hile, M. G. House, M. Fuechsle, S. Rogge, M. Y. Simmons, and L. C. L. Hohenberg, A surface code quantum computer in silicon, Sci. Adv. **1**, e1500707 (2015).
[45] J. Kelly *et al.*, State preservation by repetitive error detection in a superconducting quantum circuit, Nature **519**, 66 (2015).
[46] L. Fu, Electron Teleportation Via Majorana Bound States in a Mesoscopic Superconductor, Phys. Rev. Lett. **104**, 056402 (2010).
[47] A. Zazunov, A. Levy Yeyati, and R. Egger, Coulomb blockade of Majorana-fermion-induced transport, Phys. Rev. B **84**, 165440 (2011).
[48] S. Plugge, A. Zazunov, P. Sodano, and R. Egger, Majorana entanglement bridge, Phys. Rev. B **91**, 214507 (2015).
[49] B. Béri and N. Cooper, Topological Kondo Effect with Majorana Fermions, Phys. Rev. Lett. **109**, 156803 (2012).
[50] A. Altland and R. Egger, Multiterminal Coulomb-Majorana Junction, Phys. Rev. Lett. **110**, 196401 (2013).
[51] B. Béri, Majorana-Klein Hybridization in Topological Superconductor Junctions, Phys. Rev. Lett. **110**, 216803 (2013).
[52] A. Zazunov, A. Altland, and R. Egger, Transport properties of the Coulomb-Majorana junction, New J. Phys. **16**, 015010 (2014).
[53] A. Altland, B. Béri, R. Egger, and A. M. Tsvelik, Multichannel Kondo Impurity Dynamics in a Majorana Device, Phys. Rev. Lett. **113**, 076401 (2014).
[54] S. Plugge, A. Zazunov, E. Eriksson, A. M. Tsvelik, and R. Egger, Kondo physics from quasiparticle poisoning in Majorana devices, Phys. Rev. B **93**, 104524 (2016).
[55] P. Bonderson, K. Shtengel, and J. K. Slingerland, Decoherence of Anyonic Charge in Interferometry Measurements, Phys. Rev. Lett. **98**, 070401 (2007).
[56] P. Bonderson, M. Freedman, and C. Nayak, Measurement-Only Topological Quantum Computation, Phys. Rev. Lett. **101**, 010501 (2008).
[57] S. Plugge, A. Rasmussen, R. Egger, and K. Flensberg, Majorana box qubits, arXiv:1609.01697; T. Karzig *et al.*, Scalable designs for quasiparticle-poisoning-protected topological quantum computation with majorana zero modes, arXiv:1610.05289.
[58] M. A. Nielsen and I. L. Chuang, *Quantum Computation and Quantum Information* (Cambridge University Press, Cambridge, 2000).
[59] S. Bravyi, D. P. DiVincenzo, and D. Loss, Schrieffer-Wolff transformation for quantum many-body systems, Ann. Phys. (NY) **326**, 2793 (2011).
[60] C. Xu and L. Fu, Fractionalization in Josephson junction arrays hinged by quantum spin Hall edges, Phys. Rev. B **81**, 134435 (2010).
[61] G. Kells, V. Lahtinen, and J. Vala, Kitaev spin models from topological nanowire networks, Phys. Rev. B **89**, 075122 (2014).
[62] A. Kitaev, Fault-tolerant Quantum Computation by Anyons, Ann. Phys. (Amsterdam) **303**, 2 (2003).
[63] Z. Nussinov, G. Ortiz, and E. Cobanera, Arbitrary dimensional Majorana dualities and architectures for topological matter, Phys. Rev. B **86**, 085415 (2012).
[64] C.-K. Chiu, D. I. Pikulin, and M. Franz, Strongly interacting Majorana fermions, Phys. Rev. B **91**, 165402 (2015).
[65] D. I. Pikulin, C.-K. Chiu, X. Zhu, and M. Franz, Interaction-enabled topological phases in topological insulator-superconductor heterostructures, Phys. Rev. B **92**, 075438 (2015).
[66] A. Rahmani, X. Zhu, M. Franz, and I. Affleck, Phase diagram of the interacting Majorana model, Phys. Rev. B **92**, 235123 (2015).
[67] A. Rahmani, X. Zhu, M. Franz, and I. Affleck, Emergent Supersymmetry from Strongly Interacting Majorana Zero Modes, Phys. Rev. Lett. **115**, 166401 (2015).
[68] C. Knapp, M. Zaletel, D. E. Liu, M. Cheng, P. Bonderson, and C. Nayak, The Nature and Correction of Diabatic Errors in Anyon Braiding, Phys. Rev. X **6**, 041003 (2016).
[69] This string operator definition differs from our previous one [12], where we excluded the end-point Majorana states and referred to $\hat{W}_{ll'}$ as string operator.
[70] J. Pachos, P. Zanardi, and M. Rasetti, Non-Abelian Berry connections for quantum computation, Phys. Rev. A **61**, 010305(R) (1999).
[71] T. Karzig, Y. Oreg, G. Refael, and M. H. Freedman, A Geometric Protocol for a Robust Majorana Magic Gate, Phys. Rev. X **6**, 031019 (2016).
[72] J. R. Petta, A. C. Johnson, J. M. Taylor, E. A. Laird, A. Yacoby, M. D. Lukin, C. M. Marcus, M. P. Hanson, and A. C. Gossard, Coherent manipulation of coupled electron spins in semiconductor quantum dots, Science **309**, 2180 (2005).
[73] J. Preskill, Physics 219 Lecture Notes, Caltech (2015), http://www.theory.caltech.edu/~preskill/ph219/.
[74] Errors may occur due to poor fault tolerance of the ancilla code qubit, which is small and thus has low code distance d, cf. Fig. 5. After the injection, however, one could switch to bigger d and thereby avoid further errors.
[75] D. Gottesman, The Heisenberg representation for quantum computers, arXiv:quant-ph/9807006.
[76] M. Barkeshli and J. D. Sau, Physical architecture for a universal topological quantum computer based on a network of majorana nanowires, arXiv:1509.07135.